On the Inclusion of the Forward and Backward Silicon Tracker to the H1 track reconstruction and its Application with Charged Current

Michael Stückelberger

under the supervision of Dr. Christoph Grab and Dr. Guillaume Leibenguth

DESY, Hamburg (Germany)
September 17, 2007

Abstract

The analysis presented here compares two methods for track reconstruction for the H1 experiment at HERA. The first method (STD) defines a track only by the Central Jet Chambers (CJC) and takes space points provided by the Central Silicon Tracker (CST) for better resolution, the second method (IMP) includes additional tracks detected by the Forward and Backward Silicon Tracker (FST and BST). These methods are compared on the basis of two data samples, one without preselection and one consisting of PSeudo Charged Current (PSCC) events.

It is shown, that IMP finds much more primary vertex fitted tracks under very small and very large polar angles, but also for angles in between due to combination with central tracks. Therefore IMP improves effectively statistics and can replace STD in the official H1 reconstruction software for the next reprocessing of the HERA II data. Nevertheless, in order to do so there have to be fixed some problems of IMP with PSCC, where cuts still restrict the efficiency of IMP to below the efficiency of STD.

Contents

1 Motivation

One of the goals of the H1 experiment at HERA is to study charged current events in which the electron is transformed into a neutrino via weak interaction. In order to study these events, the position of the interaction point, where both incoming beams meet, called primary vertex, has to be known very accurately, as the kinematics of the event largely depends on it. This vertex has to be measured to the highest possible accuracy – for that reason has been built the most inner subdetector of the H1 detector, the central silicon tracker.

The behaviour of the central silicon tracker and determination of the vertices with it has been well studied and physics results using it have been published. However, there are two other detectors, forward and backward silicon tracker, which are fully operational since mid 2006 and which cover very low and very large angles that are hardly covered by other trackers. These two detectors have not been used for the determination of vertices so far.

A new code, which includes forward and backward silicon trackers has been written. It permits to determine the primary vertex with information coming from all the silicon trackers. The expected improvement is due to different reasons:

- If a track hits either the forward or the backward silicon detector in addition to another detector, the additional space points may improve the accuracy of the track reconstruction and with that the accuracy of vertex determination.
- There are found new tracks by forward and backward silicon detector, that other detectors did not see because they do not cover their small angles. These additional tracks can lead to finding new vertices: (a) because two or more new tracks can be combined to a vertex or (b) because a new track has the same vertex as origin as a track that was detected by other detectors.
- As forward and backward silicon detectors cover angles that no other detector covers, their integration in the overall analysis is a step closer to 4π sr coverage, the error due to non detected particles might be reduced.

It has to be proven, that the inclusion of forward and backward silicon detectors could lead to higher precision and/or statistics on the example of charged current analysis, since a cut is applied on the vertex position.

It might be interesting to examine, whether an improvement can be achieved in the analysis of events, in which heavy quarks are produced for a short time.

The differential cross section of Neutral Current (NC) and Charged Current (CC) is shown in figure 1.1. At large value of the transfered momentum Q^2, around $M_{Z^0}^2$, the

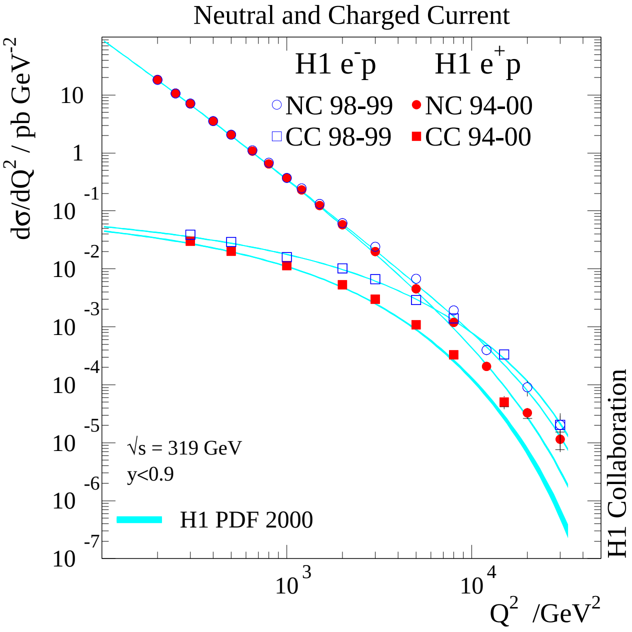

Figure 1.1: Q^2 dependence of $\frac{d\sigma}{dQ^2}$

electromagnetic and weak interactions are unified. However, the cross section is rather low, so any extension of the accessible phase space will lead to an increase of statistics. There are also improvements expected for heavy flavour physics. BST extends the charm acceptance towards low x, FST towards high x by approximately one order of magnitude each, which is the main reason why the FST has been built. With that, the charm structure function F_2^c and the beauty structure function F_2^b are expected to be measured more precisely and with higher statistics.

A quantity like F_2^s, the structure function of the strange quark might be measured using heavy quark in CC (due to Cabbibo suppression, the c quark contributes mainly). To enrich the c quark sample one could do secondary vertex studies with the new scheme.

2 Physical Processes

After an introduction to the kinematics, Charged Current (CC) interaction will be discussed in Deep Inelastic Scattering (DIS). The reason of the choice of this physical process is clear, since, as contrary to Neutral Current (NC), there is no scattered electron to define a proper primary vertex. Any improvement of the vertex efficiency will lead to an increased yield of events. The reason for the concentration on DIS is the overall goal of the analysis in hand, to determine the primary vertex and for later heavy quark studies of a secondary vertex – if there is one – as accurate as possible.

2.1 Kinematics

The four-vectors used to determine the kinematics of events (see also the feynman graphs in figure 2.1) are l and l' for the incident and scattered lepton, P and P' for the incident and the scattered hadronic state and q for the exchanged boson.
Commonly the following Lorentz invariant variables are used to describe the kinematics:

$$E_{CM}^2 = s = (P + l)^2, \tag{2.1}$$

where s is the square of the center of mass energy E_{CM}

$$q^2 = (l - l')^2, \tag{2.2}$$

where q is the four-momentum transfer. More common is the use of the positive quantity $Q^2 \doteq -q^2$. The further away Q^2 is from the mass shell, the more virtual is the exchanged boson.

$$x = \frac{Q^2}{2P \cdot q}, \tag{2.3}$$

where x is the Bjorken scaling variable. x can be interpreted as the fraction of the incident proton momentum that the interacting quark carries before the interaction.
The inelasticity, y, is given by:

$$y = \frac{P \cdot q}{P \cdot l}, \tag{2.4}$$

and can be interpreted as loss of the lepton energy relative to its initial energy in the rest frame of the proton: In this frame is $P = (M, 0, 0, 0)$ and therefore $P \cdot q = P(l - l') = M(E_l - E_l')$ and $P \cdot l = ME_l$. Therefore only in the proton rest frame is valid:

$$y = \frac{E_l - E_l'}{E_l}.$$

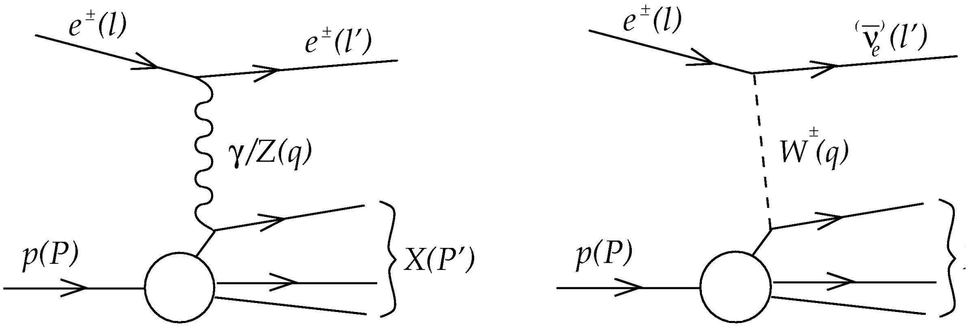

Figure 2.1: Feynman diagrams of neutral (NC) and charged current (CC) deep inelastic scattering processes. The symbols denote the particles with their four momenta in brackets. X denotes the hadronic final state [1].

Within the approximation that the scattering of the event is deep inelastic and with that $M_l, M_p \ll Q^2$ (with M_l, M_p the masses of the lepton and proton), holds

$$Q^2 = sxy. \tag{2.5}$$

The relation 2.1 is very usefull analysing events, as at known center of mass energy E_{cm} (provided by the accelerator) any two of the three variables x, y and Q^2 are sufficient to describe the DIS kinematics (overconstrained system).
There are different methods how one can get these parameters out of experimental data – some of them are well described in [1].

2.2 Deep Inelastic Scattering (DIS)

Inelastic scattering is called deep, if the masses of the incident particles are negligible small compared to Q^2 or to qP (see section 2.1 for explanation of the variables). At HERA (here stood the detector H1 [2] of which the analysed data are from; see section 3 for more details), DIS events are those, where the electron or positron has enough energy to interact not only with the proton seen as a pointwise particle but with its constituents, the quarks. As a result, a lepton and a multihadronic final state are produced. So in fact, DIS is only inelastic scattering with regard to scattering on the whole proton but elastic with respect to scattering on a single quark.
Possibilities for such DIS events are:

- Neutral Current (NC) events, which are mediated by γ or Z^0 boson exchange and where type and charge of the lepton in the final state does not differ from the incident lepton, and
- Charged Current (CC) events, which are mediated by W^+ or W^- boson exchange and where the incident lepton is changed to the corresponding neutrino.

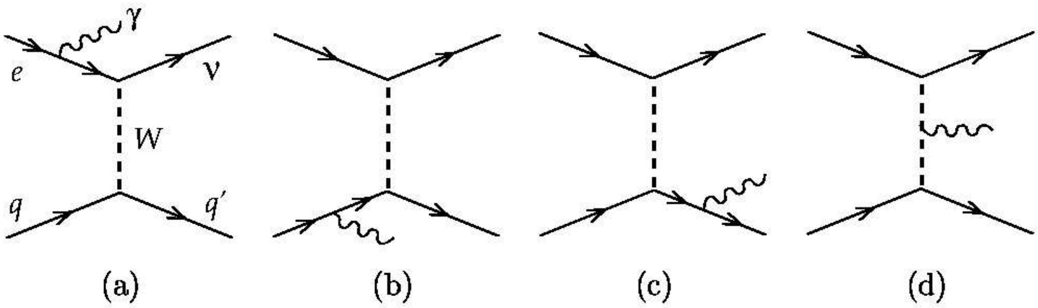

Figure 2.2: Feynman graphs for second order charged current events due to emission of a photon: from the incident electron (a) or quark (b), from the outgoing quark (c) and from W (d) [1].

The generalized reactions for NC and CC events and the corresponding exchanged particles are the followings:

$$ep \to eX \qquad \text{neutral current event with exchange of } \gamma \text{ or } Z^0, \tag{2.6}$$

$$ep \to \nu X \qquad \text{charged current event with exchange of } W^{\pm}. \tag{2.7}$$

Herein denotes X a not specified hadronic final state. Feynman diagrams of these two reactions are shown in figure 2.1.
While NC events can occur due to electromagnetic interaction by exchange of a photon (γ) or due to weak interaction by exchange of a Z^0-boson, CC events are always a result of weak interaction by exchange either of a W^+ or of a W^--boson. The tracks of the electron and of the hadronic final state seem to origin from the same vertex, the interaction point.

2.3 Experimental Aspects

In this section the signature of charged current events in the experiment will be discussed, but also the signature of background processes and how to differentiate between CC events and background. Finally the problem of low statistics of CC (see figure 1.1) is discussed and how CC events can be studied in some more detail using Pseudo Charged Current (PSCC) events.

2.3.1 Signature of Charged Current (CC) Events

The feynman graph of a CC event shown in figure 2.1 is only leading order. But also higher orders contribute to the CC cross section – a discussion of them with all formulas is given e.g. in [1] and the literature mentioned there. Here only QED corrections are discussed, as can be seen in figure 2.2 representing the feynman graphs of the second order events with emission of an additional photon.
The γ radiation from the incident particles (a) and (b) is usually called Initial State Radiation (ISR), the radiation from the outgoing particles (d) Final State Radiation

(FSR). FSR can in CC in contrast to NC events only come from the quark, as the outgoing lepton (ν) is uncharged.
The typical signature of a CC event is the following:

- *Missing transverse momentum* because of the ν that escapes the detector. Overall missing momentum is no criterion, as the momentum the interacting quark carries is not known (only the momentum of the proton), and the hadronic rest of the proton escapes the detector through the beam pipe.
- *High momentum transfer*: Typically charged current events have a momentum transfer $Q^2 > 100$ GeV^2.
- *Back to back topology*: In contrast to γp reactions that are distributed isotropically around the beam axis, the neutrino is scattered in the opposite direction of the struck quark.

2.3.2 Background Processes to Charged Current

As the current analysis does not include the differentiation between charged current and background that has been done earlier in [1], it is only resumed here, which processes contribute most to the background of CC events.

- Photoproduction ($ep \rightarrow e\gamma p$): Specially for low Q^2 the dominant process that can exceed CC events for several orders of magnitude. It can mimic a CC event if particles from a hadronic final state (e.g. ν) escape detection.
- Lepton pair production ($ep \rightarrow el\bar{l}X$): If l is a μ that deposits not much energy in the detector, or a τ that decays into $\mu\nu\bar{\nu}$, they can mimic a CC event.
- W production ($ep \rightarrow eWX$): A rare process, where a real $W^{\pm}$ is produced. If the W boson decays leptonically, it can mimic a CC event due to the momentum carried by the neutrino.

What can always contribute to background for CC are events, where particles are not detected because of imperfections of the detector (dead material, not complete 4π sr coverage).

2.3.3 Pseudo Charged Current (PSCC) Events

In order to get charged current data with of high accuracy, one first has to understand the detector with its efficiencies of detecting charged current events very precisely. The problem herein is, that statistics of CC data alone is not sufficient as CC events are for low Q^2 suppressed by the propagator mass (M_W) according to the formula [1,11] for the differential cross section of CC events in electron proton collision,

$$\frac{d^2\sigma_{CC}^{e^{\pm}p}}{dxdQ^2} = \frac{G_F^2}{2\pi x}\left(\frac{M_W^2}{Q^2 + M_W^2}\right)^2 \Phi e^{\pm} p_{CC}, \tag{2.8}$$

with the Fermi constant G_F and the reduced CC cross section $\Phi e^{\pm} p_{CC}$.
In the case of neutral current, only the part of the cross section due to weak interaction (with M_{Z^0} as propagator mass) is suppressed, but not the cross section due to electromagnetic interaction, which results [1,11] in an overall NC cross section

$$\frac{d^2\sigma_{NC}^{e^{\pm}p}}{dxdQ^2} = \frac{2\pi\alpha^2}{xQ^4}\Phi e^{\pm} p_{NC}, \tag{2.9}$$

with the electromagnetic coupling constant α and the reduced NC cross section $\Phi e^{\pm} p_{NC}$.
Therefore, the NC event rate exceeds the CC event rate for low Q^2 by more than two orders of magnitude. As the scattered electron in NC events can be detected very efficiently and its track reconstructed with high precision (for the data see [12]), the high statistics of NC events provides the possibility to perform detailed detector quality checks [1].
They are in charged current analysis used:

- to calibrate the hadronic energy,
- to determine the distribution of the vertices in order to adjust the vertex distribution of the CC simulated events and
- to produce so called pseudo charged current events in order to determine the efficiencies of the CC selection requirements.

These pseudo charged current (PSCC) events are created artificially by removing the electron track of NC events (that can be either data or Monte Carlo simulation events).
As the neutrino of CC events is not detected anyway, PSCC events look in the detector the same as CC events (compare also the feynman graphs of PSCC and CC events in figure 2.3). While the missing momentum in CC events is due to the escaping neutrino, the missing momentum in PSCC events is due to the removed scattered electron. Therefore, PSCC events are well suitable to provide more statistics of CC events for calibration.
Nevertheless, due to radiative effects within NC events that appear in PSCC as well [13], a slight difference between PSCC and CC events remains. This is considered in the systematic error [1].
In the following it is described how the PSCC procedure of removing an electron from NC events works [1]: First is applied the electron finding algorithm to each selected NC event that shall be converted to a PSCC event. Next, all relevant detector information that is supposed to be due to the electron is removed from the event. This is all information found in the $\eta - \varphi$ cone with the radius $R_{\eta-\varphi} = 29°$, corresponding to the electron cluster given by the liquid argon calorimeter (LAr). Here, $\eta = -\ln(\tan(\theta/2))$ is the pseudorapidity and $R_{\eta-\varphi}$ is defined as

$$R_{\eta-\varphi} \doteq \sqrt{\Delta\eta_{tracks}^2 + \Delta\varphi_{tracks}^2}. \tag{2.10}$$

The kinematics of the new PSCC event have changed by the removal of the electron with respect to the original NC event. Therefore, one must recalculate all the kinematics of

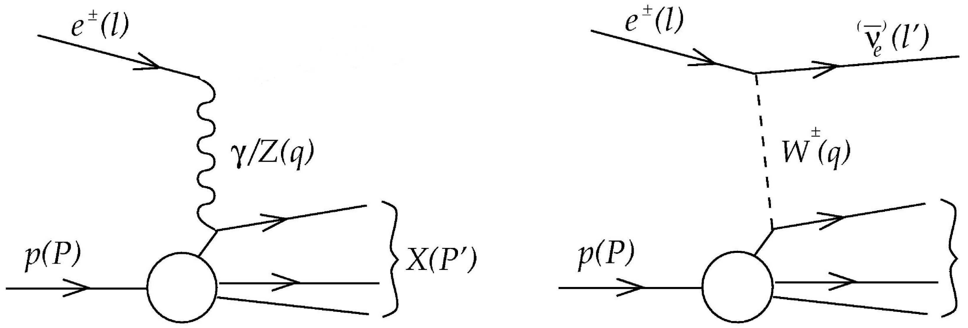

Figure 2.3: Feynman diagrams of pseudo charged current (PSCC) and charged current (CC) events. It can be seen, that the detected particles are the same.

the event. In order to do so, the reconstruction (via h1rec [9,10]) is rerun on the PSCC event.

Finally, each PSCC event gets a weight, which is defined as

$$w(x, Q^2) = \frac{d^2\sigma_{CC}}{dxdQ^2} / \frac{d^2\sigma_{NC}}{dxdQ^2}, \tag{2.11}$$

to adapt it to the CC cross section, so that the expected kinematic distributions are reproduced. A PSCC event that was produced out of a NC event can be seen in figure 2.4.

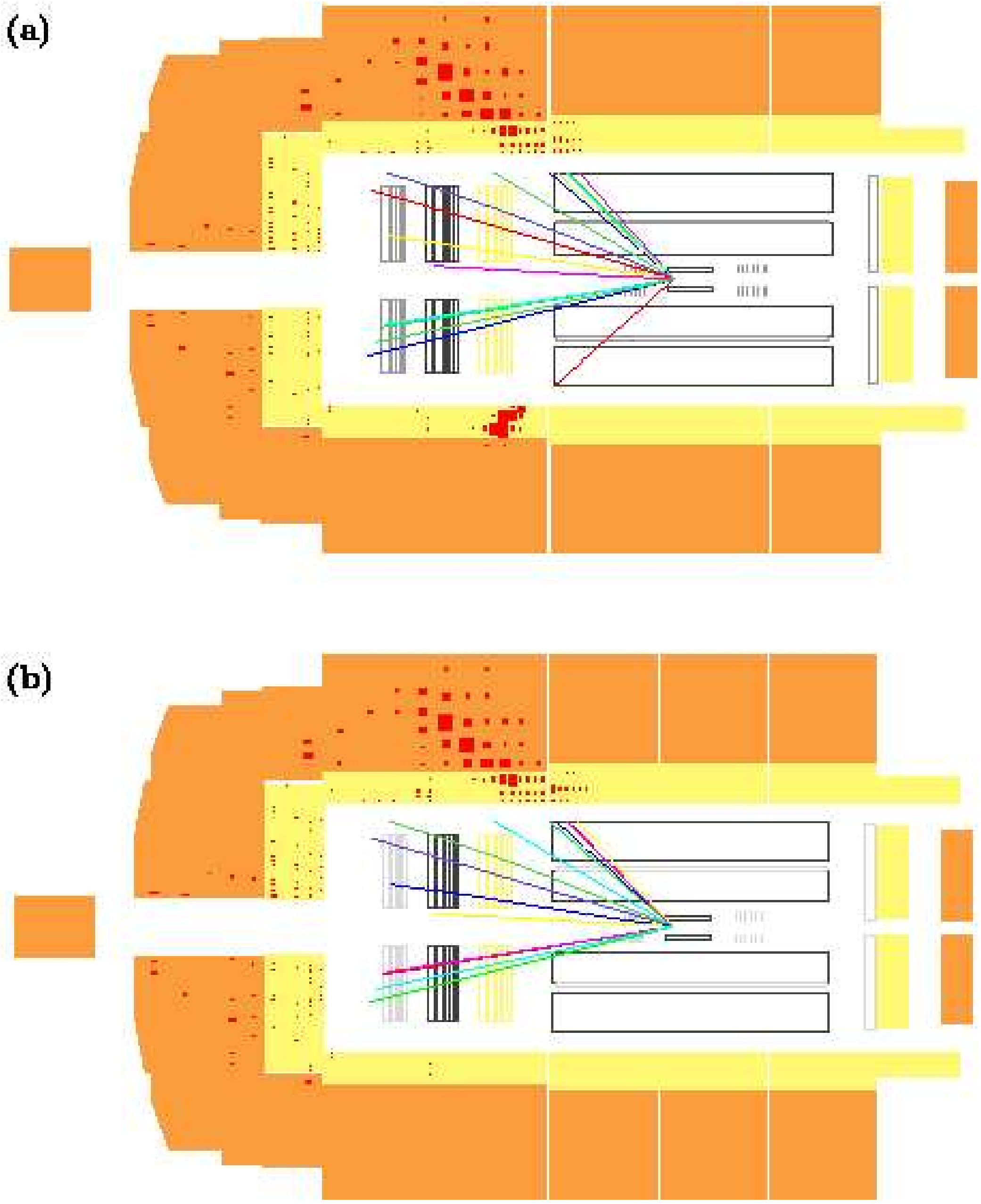

Figure 2.4: Side view of the H1 detector with a NC event before (a) and after (b) the electron removal (PSCC) [1].

3 H1 Experiment

After a short introduction to the accelerator HERA, an overview over the H1 detector with a more detailed discussion of the tracker system in this chapter will be given.

3.1 HERA Accelerator

HERA (Hadron Elektron Ring Anlage (see figure 3.1)) is an accelerator located at DESY (Deutsches Elektronen SYnchrotron) in Hamburg, Germany. It consists of a hadron and an electron ring which are in the same tunnel of 6.3 km circumference. After running from 1992 until the end of 2000 (HERA I), it was upgraded and started again in the year 2001 (HERA II). All data used in this analysis is from HERA II, therefore only those specificatons are given here. The main purpose of the upgrade was to increase the luminosity, which is defined as

$$\mathcal{L} = \frac{f N_e N_p}{4\pi A}, \qquad \left[\frac{1}{cm^2 s}\right], \tag{3.1}$$

where f stands for the frequency, with which bunches collide, N_p and N_e are the numbers of protons and electrons respectively per bunch and A is the cross section of the beam. Usually, $\mathcal{L}$ is measured in $\frac{1}{cm^2 s}$. It is linked to the reaction cross section σ and to the event rate $\dot{N} = \frac{dN}{dt}$ via

$$\dot{N} = \sigma \mathcal{L}. \tag{3.2}$$

If one is dealing with absolute numbers of events N, the integrated luminosity $L = \int \mathcal{L} dt$ is used for $N = \sigma L$.

Another important improvement was the polarization of the electron beam. By the emission of synchrotron radiation, electrons become transversaly polarized. With the spin rotators installed for HERA II, a tranversal polarization of ≈ 40 % was achieved. Protons have been accelerated up to 920 GeV. Alternatingly electrons and positrons have been accelerated up to 27.55 GeV. In the proton ring as well as in the electron[1] ring there could be stored up to 210 bunches. The bunches contained each 10^{11} particles and were separated by 96 ns time intervals.

The proton-electron collisions took place in two opposite interaction points: in the north in the experiment H1 and in the south in the experiment ZEUS. Both are general purpose detectors. The center of mass energy that could be reached in these collision points was up to $\sqrt{s} = 318$ GeV.

---

[1] The lepton in the HERA machine is either an electron or a positron. In the following, the lepton beam will be named electron.

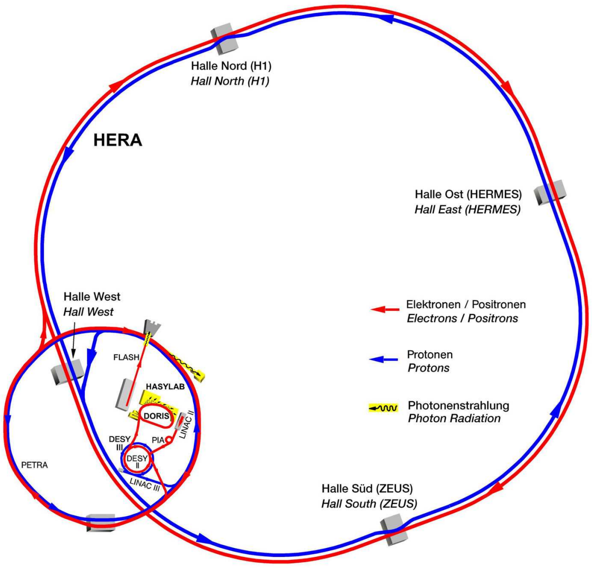

Figure 3.1: Schematic view of the DESY accelerator system, the HERA ring with the location of the experiments and its preaccelerators [1].

Beside these two big collider experiments, there have been working two fixed target experiments: HERMES in the eastern and HERA-B in the western part of HERA. Hermes, which had a spin rotator already during HERA I, has been used mainly to examine the spin structure of the photon, whereas HERA-B was built to produce mainly final states with b quarks.

3.2 H1 Detector

In contrast to most collider detectors, H1 is built asymmetrically, as the remaining particles of ep interactions that have to be studied are boosted towards the proton direction. Corresponding to that are chosen the coordinate systems: z points into the forward direction i.e. into the direction of the proton, x points to the center of the HERA ring and y points upwards. The azimuthal angle φ is defined in the xy plane, the polar angle θ in the rz plane (see also figure 3.2).

A schematic view of the HERA detector is given in figure 3.2. In the center of H1 there is, after the beam pipe $\boxed{1}$, the Central Track Detector (CTD) $\boxed{2}$.

Within the superconducting coil, there are also the electromagnetic $\boxed{4}$ and hadronic $\boxed{5}$ calorimeters with Liquid Argon as scintillator (LAr). Outside the superconducting coil $\boxed{6}$ are the Muon Chambers $\boxed{9}$.

In the forward direction there is the Forward Tracking Detector (FTD) $\boxed{3}$ followed by Liquid Argon calorimeters (LAr) whereas in the backward region there are the electromagnetic and hadronic Spaghetti Calorimeters (SpaCal) $\boxed{12}$.

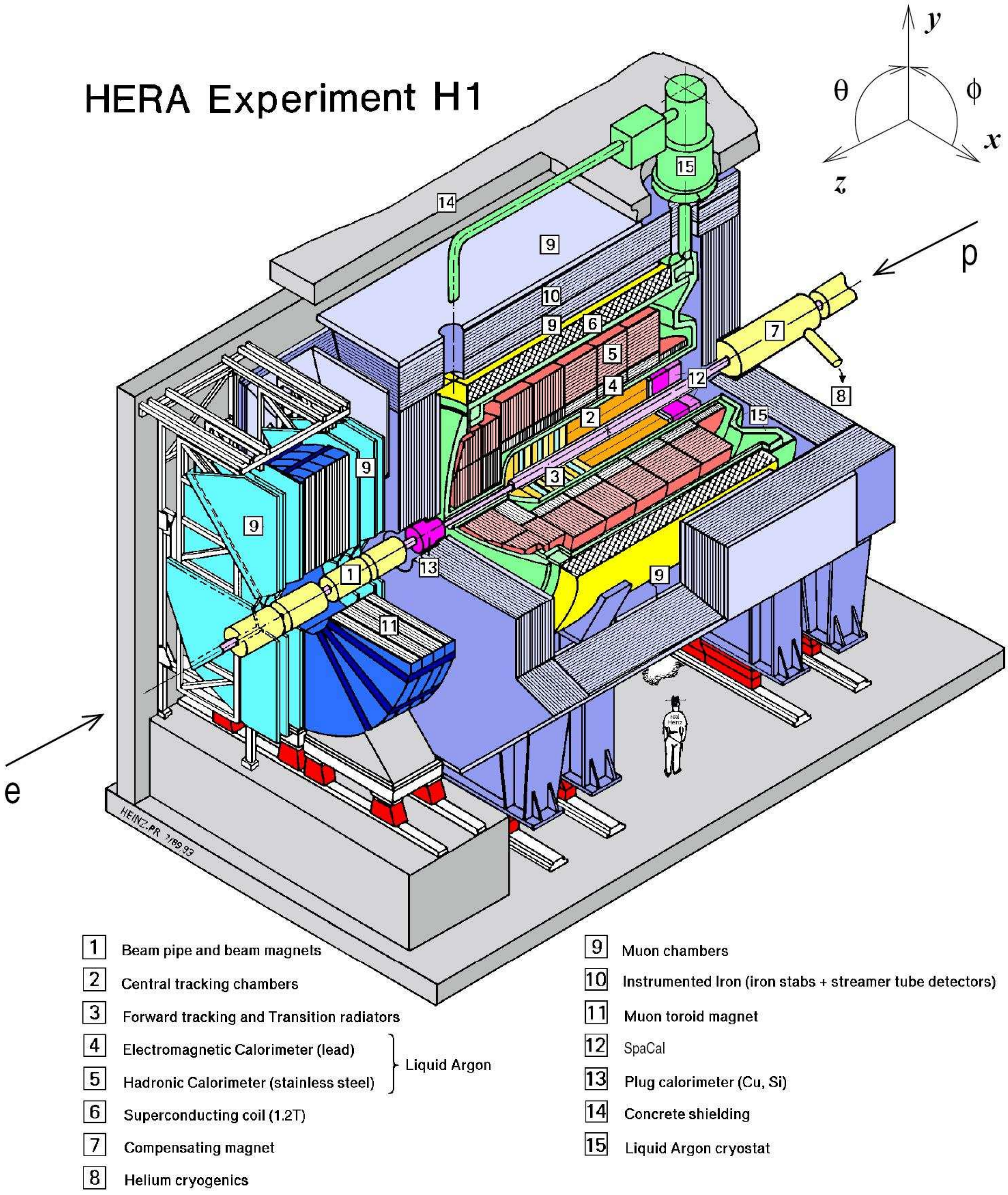

Figure 3.2: Schematic view of the H1 experiment [1].

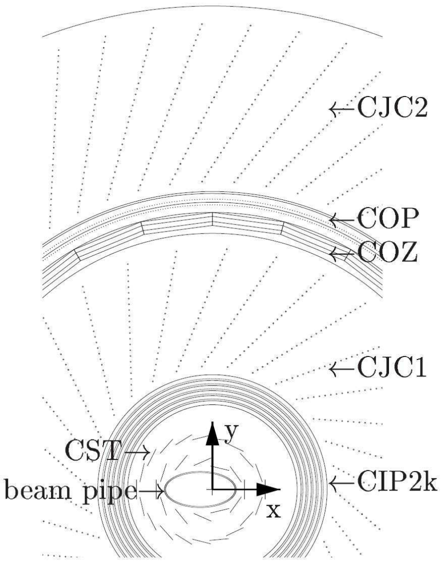

Figure 3.3: $r\varphi$ cut of the Central Tracking Detector with all subdetectors [1].

3.2.1 Central Tracking Detector (CTD)

The purpose of the CTD is mainly to measure the track and the momentum of charged particles coming from the interaction region. As the superconducting coil provides a B field along z, the tracks of charged particles will describe curvatures in the xy plane according to the formula

$$p_T = qBr, \tag{3.3}$$

where is p_T the transverse momentum of the particle, q the charge of the particle, B the external magnetic field and r the curvature radius. Measuring at least 3 points of a track, the curvature radius can be determined and therefore the momentum can be calculated.
The CTD consists of the following subdetectors (from the beamline outwards): The Central Silicon Tracker (CST), the Central Inner Proportinal chamber (CIP2k) (replacing in the upgrade 2001 the Central Inner Z-drift chamber (CIZ) and the old CIP), the Central Jet Chamber (CJC1), the Central Outer Proportional chamber (COP), the Central Outer Z-chamber (COZ), and another Central Jet Chamber (CJC2).
The arrangement of these subdetectors can be seen in a $r\varphi$ cut in figure 3.3.
As this report is a study of the reconstruction of tracks, only the relevant subdetectors used in the reconstruction will be described in more detail in the following.

Central Jet Chambers (CJC)

The CJC consists of two coaxial drift chambers with sense wires parallel to the z axis. The inner drift chamber CJC1 has 24 layers of sense wires in each of the 30 drift cells

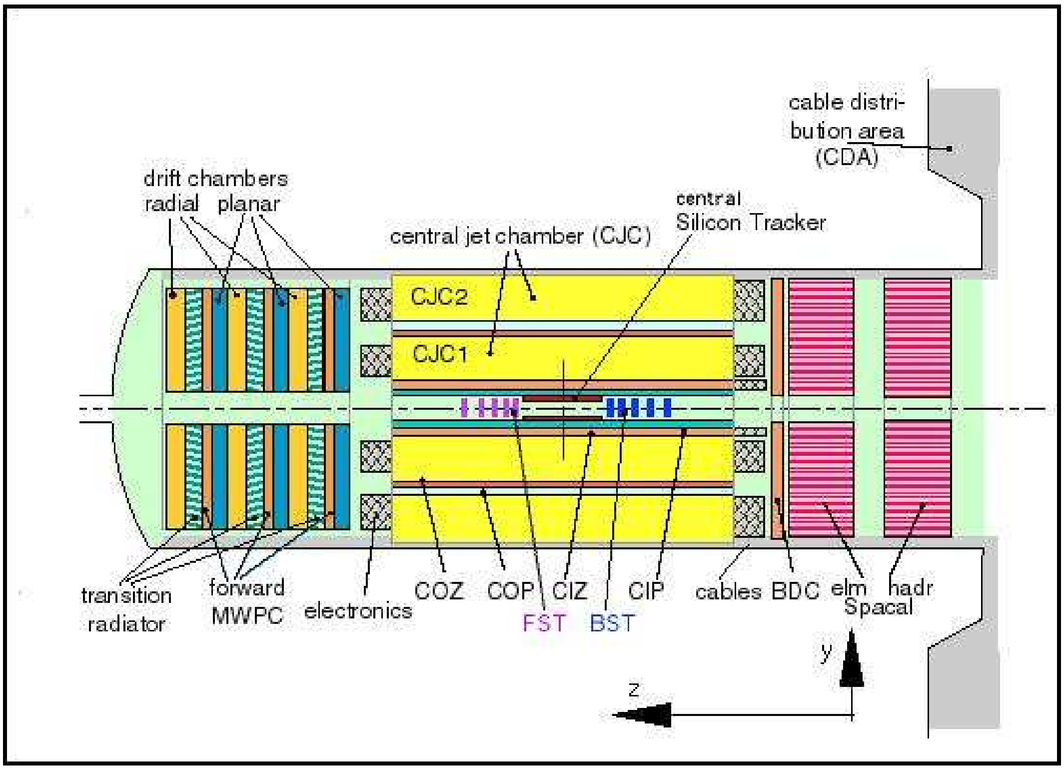

Figure 3.4: Schematic view of tracker system of the H1 detector [1].

regularly distributed in φ, the outer chamber CJC2 has 32 layers in each of the 60 cells [2]. To increase the resolution, the cells are tilted by about 30 °, therefore ionisation electrons and ions travel perpendicular to the track direction.
CJC1 is sensitive for -112.5 cm $\leq z \leq 107.5$ cm and for 21.8 cm $\leq r \leq 42.6$ cm, CJC2 for -112.5 cm $\leq z \leq 107.5$ cm and for 54.5 cm $\leq r \leq 82.3$ cm.
During operation, the resolution of the CJC detector has been ameliorated to $\sigma_{dca} <$ 200 µm in $r\varphi$ for transverse momenta above 1 GeV and to $\sigma_{Z_0} < 0.87$ cm in z.

Central Silicon Tracker (CST)

The main purposes of the CST [3] are to improve the accuracy of track measurement with special remark on vertex determining and to study heavy flavor physics via the extraction of lifetime information throught secondary decays.
The CST is the innermost detector. Figure 3.4 shows how the CST is positioned with relation to the other trackers. It is much smaller than the CJC but covers due to its closeness to the interaction region a similar polar angle as the CJC.
The CST consists of two layers of 12 and 20 ladders which are highly irregularly arranged in r due to the elliptical shape of the beam pipe and the non-centered position of the interaction region. The inner layer is positioned right near the beampipe (and is therefore

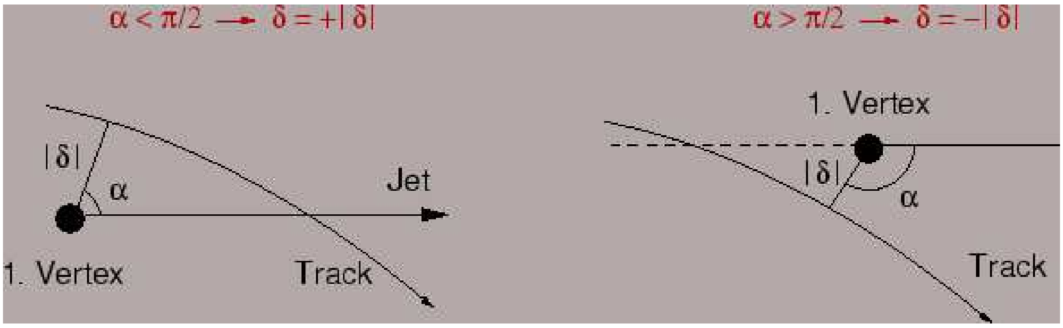

Figure 3.5: Description of the impact parameter δ (Distance of Closest Approach (*dca*) [14]

of the same elliptical shape as the beampipe) to get data as close as possible to the interaction point. The outer layer is positioned in the remaining place, as far as possible away from the interaction point to have a larger level arm.

The ladders are placed such that straight tracks coming from the interaction region pass the ladders perpendicularly. Each ladder is built of 6 double sided silicon strip sensors with p-type strips parallel to the z axis and n-type strips perpendicular to the z axis in order to provide high accuracy in φ as well as in z. Three sensors are bonded together to form a half-ladder which is read out by one hybrid at the end. Each side of the hybrid contains five APC128 chips which are read out serially. A picture of the CST before being inserted in the H1 detector can be seen in figure 3.6. The geometry with the different coordinate systems and the corresponding transformations of the CST (including alignment corrections and calibration) is given in detail in [8].

The achieved resolution is 12 μm on the p-doped side and 22 μm on the n-doped side, which results in an impact parameter resolution of 37 μm for high momentum tracks. The impact parameter δ is defined as the Distance of Closest Approach *dca* for a track that is not fitted to the primary vertex. It is the length of the vector that is orthogonal to the track and points to the primary vertex (see also figure 3.5) [14]. Large values of the impact parameter exhibit lifetime information, which can be used to distinguish heavy quarks from lighter ones.

The average hit efficiency is 97 % for the p-side and 92 % for the n-side [3, 7].

The sensors are of 300 μm thickness which corresponds together with the other CST material to a total energy reduction of a particle of 1.4 % X_0 in the central region [4].

The CST is sensitive for -17.8 cm $\leq z \leq$ 17.8 cm and covers φ completely for 2π due to an overlap of the ladders.

The CST is delivering space points. After having reconstructed a CJC track, it is propagated through the CST. A simple χ^2-technique (no Kalman filter as for BST/FST) is used to link a CST space point to a CJC track. Therefore, the linking of the CST to the CJC tracks does not change the track itself, only the five parameters dca, φ, z, θ and $\kappa(\propto p_T^{-1})$ are adapted. Energy loss correction, accounted for each layer of silicon is applied before the linking. As a result, only the parameters of the trajectory are changed, but not the starting radius of the track (the start radius remains the one of the first CJC

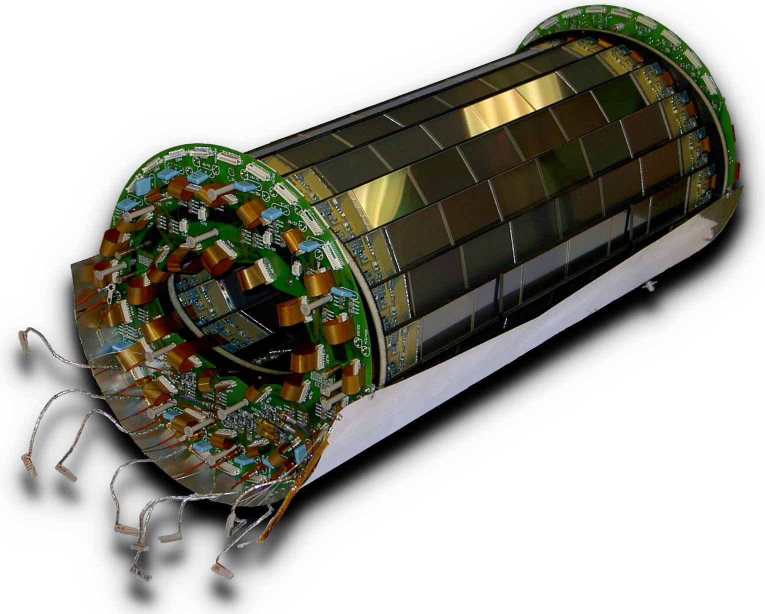

Figure 3.6: The CST before being inserted in the H1 detector.

hit). More information about reconstruction of CST tracks can be found in [9,10].

3.2.2 Backward and Forward Silicon Trackers (BST and FST)

The position of the BST and the FST relative to the other trackers is shown in figure 3.4.
The final version of the BST (2003-2007) [20] consists of 6 wheels right around the beam pipe where the protons are coming from. Each wheel contains 24 sensors with always 2 sensors mounted back to back; As each sensor has only one dimensional readout, by rotating the sensors by $\frac{\pi}{2}$ against each other they provide a high two dimensional resolution. In contrast to the CST, the sensors of BST and FST are mounted perpendicularly to the beam. The 12 sensor pairs cover $\frac{3}{4}$ of the azimuthal angle; $\frac{1}{4}$ is occupied by the beam pipe. (During HERA upgrade 2001, where the shape of the beampipe had been changed from cylindrical to elliptical, the originally concentric BST with 16 sensors per wheel covering $0 < \varphi \leq 2\pi$ was addapted to the beampipe and 4 sensors had to be removed, see figure 3.7. While BST consisted of 8 wheels from 2001 to 2003, two of them had to be removed due to radiation damage.)
On the back of 4 of the 6 wheels are mounted pad triggers (before 2003: 8 pad triggers), that provide a fast input for trigger level 1 [2,4].
The FST is a mirror of BST but smaller. Instead of 6 wheels it contains only 5 and does not deliver trigger signals [5].
The resolution of the FST and BST sensors is 16 µm. Both FST and BST provide enough

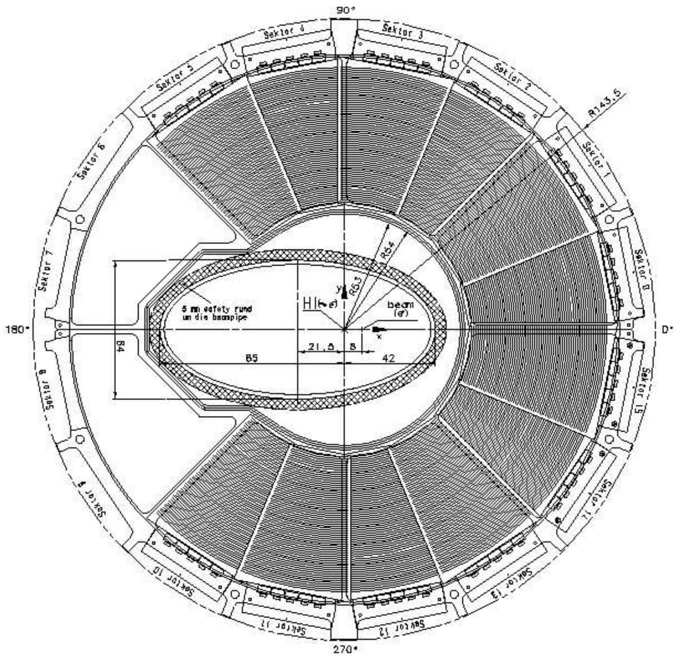

Figure 3.7: $r\varphi$ view of one wheel of the BST [5].

space points to reconstruct tracks out of them without the need of any other detector. Combined tracks of the Forward Track Detector (FTD) and FST might achieve impact parameter resolutions in $r\varphi$ of 90 μm which is well below mean decay lengths of charm and beauty particles that are e.g. 150 μm(D^0), 450 μm(D^+) and 700 μm(B) [5].

4 Analysis and Results

Firstly, the different algorithms for the track reconstruction will be presented. Secondly, the analysis procedure will be described and then finally, the results will be presented.

4.1 Algorithms for Track Reconstruction

Two event reconstruction streams that serve as input for the current analysis will be discussed. Both contain the same events, but their tracks are reconstructed by the routine h1rec [18] differently. In the older configuration, all tracks have been constructed only using data from CJC and CST according to (a) of figure 4.1. Such tracks are called CSKR tracks. Since there is no vertex fit applied at this stage of the reconstruction, these tracks are, in the H1 jargon, called CJC-CST non vertex fitted tracks: The CJC defines a track (using the subroutine cjcrec), that was reprocessed through the CST (using cstrec). The result are tracks with high precision due to the combination of CST and CJC, but all the tracks that are produced under a very small or very large angle θ are lost as none of CST and CJC cover these polar angles.

Here the new algorithm should lead to an improvement. For generating the new event sample, according to (b) of figure 4.1, the reconstruction routine h1rec called also first cjcrec. But before calling cstrec, the events are processed through a package provided by S. Gorbounov [19] that includes FST and BST hits to the CJC non vertex fitted track. The output of this package is a set of tracks, which contain information of CJC-FST-CST or CJC-BST-CST or of parts of them. Not all three detectors need to have hits to define a track. The generated tracks by this software are called CBFR tracks. Integrating FST/BST in the analysis is far more difficult than integrating the CST, as the geometry is completely different: Whereas CST and CJC have coplanar sensors and wires (therefore the covariance matrices can be combined easily), this is not the case for FST/BST where a Kalman filter has to be used.

The actual analysis is done by a routine using h1oo [15, 16], which is built on root [17]. The whole analysis is done once for non vertex (NPV) fitted tracks and once for primary vertex (PV) fitted tracks. The primary vertex fitted tracks are obtained by adding information of the primary vertex to a given track, leading to an improvement of the track parameters due to the fact that the primary vertex is well measured.

4.2 Cuts and Binning

All relevant detectors have to be ready for data taking to accept an event, meaning that the high voltage is on and all tracking detectors are readout (except the FTD).

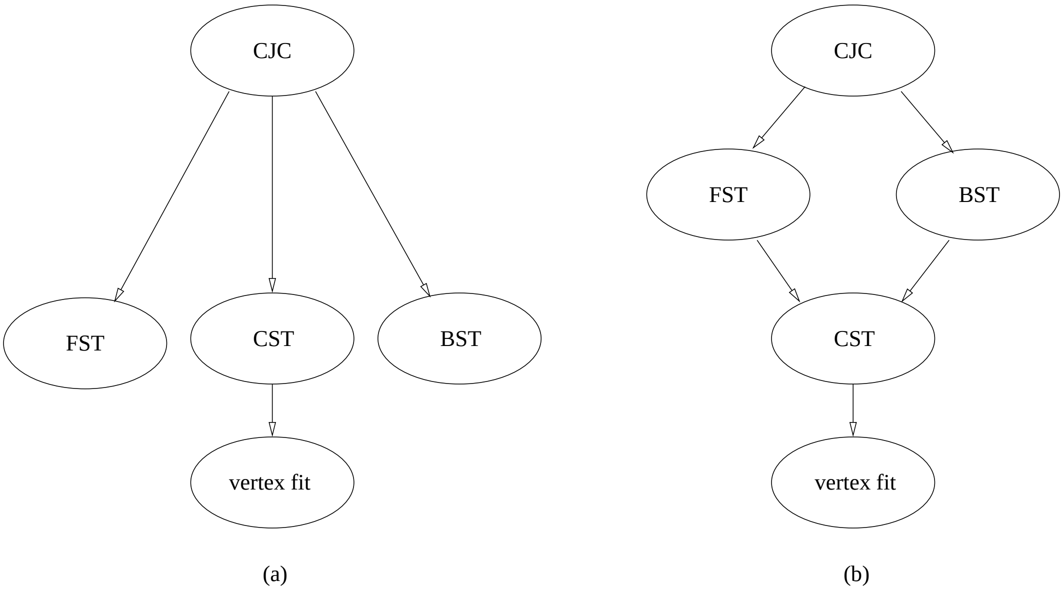

Figure 4.1: Diagram of track reconstruction: As it has been done so far (a) and after implementation of FST/BST hits (b).

To accept tracks of an event (event cut), the event must have at least one non vertex fitted central track. This cut has been chosen due to the fact, that the reconstruction routine for FST/BST tracks is not implemented yet in the central tracks.
The track cuts are:

- *Transverse momentum p_T (for NPV and for PV)*: All the analysis has been done for five different cuts of p_T in order to see differences between different momentum ranges:
  - $p_T > 120$ MeV
  - $p_T > 300$ MeV
  - $p_T > 500$ MeV
  - $120 \text{ MeV} < p_T < 300$ MeV
  - $300 \text{ MeV} < p_T < 500$ MeV

  If an electron has a p_T below 120 MeV, its curvature is so strong due to the magnetic field that it spools up without ever reaching the CJC which is always required to have at least one hit (by the reconstruction software).

- *Start radius (for NPV and for PV)*: The start of the track has to lie within a zylinder of the radius $r_0 < 50$ cm. Tracks, that do not fulfill this criterion, leave their first signal only in CJC2 which results in very inaccurate vertex determination. Also, it is quite probable that such tracks do not have the primary vertex as origin.

- *Impact parameter dca (for NPV only)*: As a first step, charged current data is analyzed, where all tracks are fitted to the primary vertex. In order to reduce other events with secondary vertices, the impact parameter cut is set to $dca < 5$ cm. This is the only track cut that has been set for NPV but not for PV tracks, as dca is for PV tracks by definition 0 within the resolution.

4.2.1 θ-Binning

In order to see which sub-detector might contribute to a change in efficiency, a θ binning is chosen in such a way that the binning is not equidistant in radians, but corresponds to sensitive parts of the detectors [either partially sensitive (detector stands in the table in brackets) or fully sensitive (without brackets)]. The list of all θ bins with the sensitive subdetectors is shown in table 4.1.

Bin nr.	$\theta_{start}[°]$	$\theta_{end}[°]$	Active detectors
0	0	6.674	No sensitive detector
1	6.674	9.536	(FST)
2	9.536	11.464	FST
3	11.464	12.358	FST-(CST1)
4	12.358	13.387	FST-(CST)-(CJC1)
5	13.387	18.865	(FST)-(CST)-(CJC1)
6	18.865	21.617	(CST)-(CJC1)
7	21.617	26.884	(CST)-CJC1
8	26.884	30	(CST)-CJC1-(CJC2)
9	30	37.437	CST-CJC1-(CJC2)
10	37.437	143.812	CST-CJC1-CJC2
11	143.812	150	CST-CJC1-(CJC2)
12	150	154.152	(CST)-CJC1-(CJC2)
13	154.152	159.305	(CST)-CJC1
14	159.305	162.654	(CST)-(CJC1)
15	162.654	167.642	(BST)-(CST)-(CJC1)
16	167.642	168.767	(BST)-(CJC1)
17	168.767	169.033	BST-(CJC1)
18	169.033	171.270	BST
19	171.270	171.423	(BST)
20	171.423	180	No sensitive detector

Table 4.1: θ binning and the corresponding sensitive detectors. Those in brackets are partially sensitive.

4.3 Results

The goal of this analysis is to compare two sets of events. In the following, the first set of events will be called standard (STD), which is implemented in the official h1 software (CSKR tracks, considering CJC and CST hits), the latter will be called improved (IMP), which considers in addition to STD also FST/BST hits (CBFR tracks). More details can be found in section 4.1.
In the previous section it is explained how the two set of events are generated.
Only the analysis with the transverse momentum cut $p_T > 500$ MeV will be presented here, as all important effects can be seen herein.

4.3.1 Comparison of Inclusive Events

The data analysed in this section have been taken on one day in december 2006 by the H1 experiment with an integrated luminosity of $153\,\mathrm{nb}^{-1}$ (inclusive sample). In the following the two reconstruction methods STD and IMP are compared. The bars always denote STD, the points IMP data. In the comparison no normalization has been applied.
First it is shown in figure 4.2, that both data sets contain effectively the same runs and select exactly the same number of events. With that, the pre-condition for the data being comparable is met.
Next is analysed the z position of the vertex, z_0. Figure 4.3(a) shows the expected symmetric distribution around $z_0 = 0$ with a large peak in the center for non vertex fitted STD as well as IMP tracks, bot not for primary vertex fitted (figure 4.3(b)). By default, z_0 is set 0 (without any physical meaning), if the vertex is not determined. That explains, why the peak does not appear for PV tracks, as their vertex position is known by definition (within resolution).
Also the transverse momentum p_T (see figures 4.4(a) and 4.4(b)) agree perfectly with the expectations. In particular IMP shows the very same distribution as STD – this is also an important condition for replacing STD by IMP. Why IMP finds more PV tracks than STD but not more non vertex fitted tracks will be explained later. Tracks with p_T below 500 MeV are cut in order to be less sensitive to resolution effects of the CJC.
The relative quality of tracks can be seen plotting the function ProbChi (see figures 4.5(a) and 4.5(b)). ProbChi denotes the probability that an observed χ^2 exceeds the determined χ^2 by chance. In former analysis the distribution used to be flat – why it is not the case here has to be examined further. The problem has been traced back to an improved energy loss correction. However, STD and IMP show the same behavior.
In figures 4.6(a) and 4.6(b) the radius is shown, where a track starts, which is the distance between the origin of H1 coordinate system and the first hit in a tracker detector in $r\varphi$ plane [except CST: As CST provides at most two space points (only two sensor layers), it can not define a stand alone track.]. While the shape of IMP corresponds in general well to the shape of STD it can be seen very nicely that IMP has additional tracks that start at a smaller radius than all other tracks. These tracks hit FST/BST; The start radius of ~ 6 cm for FST/BST tracks does not correspond to the physical distances but is set to that value. Details about this setting still have to be clarified.

The larger peak seen for both NPV and PV, for STD and for IMP corresponds to the minimal radius of CJC1. The CST does not define the start of a track, which is due to the chosen algorithm (see section 4.1): Only CJC and FST/BST define tracks (and with that their starting points), whereas CST improves their accuracy by adding space points.
Figure 4.7(a) and 4.7(b) display the azimuthal angle φ track distribution of non vertex fitted and PV tracks respectively. The bins are chosen such, that each bin covers exactly one segment of the BST/FST. The typical distribution with the two wide peaks is due to the elliptical shape of the beam pipe.

Nevertheless, the relatively flat distribution (zero suppressed) is somewhat unexpected for the IMP tracks, as 4 segments of FST/BST are missing and the remaining ones cover only 270 degree. In fact IMP shows in the 4 segments around π significantly less entries than STD. The fact, that in these bins are still that many entries can be explained by the definition of φ: φ is measured at the vertex. Due to the magnetic field, the electrons are drifted in φ (by a variable $\Delta\varphi$ that depends on the particles momentum) and reach FST/BST under a different φ as they started. This way, active segments detect electrons with a starting angle φ that is not covered by the FST.

The distribution of the polar angle θ is shown in figures 4.8(a) and 4.8(b). For non vertex fitted tracks the distributions are not exactly the same, for some angles IMP selects less tracks than STD as could already be seen in former diagrams. One reason could be, that IMP selects additional tracks detected by FST/BST, which can fit to a non vertex fitted track detected by CJC in STD, so that the central track is in IMP a PV track. In fact it can be seen in figure 4.8(b), that also for central tracks, where FST/BST are not sensitive, additional IMP tracks are found. Under FST/BST sensitive angles the number of IMP tracks exceeds the number of STD tracks by far.

These plots demonstrate, that IMP has the potential to replace STD for the next reconstruction of all HERA II data where FST and BST are running.

In order to examine in more detail which detectors contribute to the improvement and what still can be improved, the plots 4.8(a) and 4.8(b) have been done with a special binning (see section 4.2.1 for details).

For each single bin plots with the φ and the p_T distribution have been generated. Examples of such plots can be seen in figures 4.10(a), 4.10(b), 4.11(a) and 4.11(b). The former two plots show the azimuthal angle φ distribution in the θ bin, where only FST is sensitive, the latter two the transverse momentum p_T distribution in the θ bin, where only BST is sensitive. One can see, that FST and BST provide effectively only additional tracks to PV.

The entries of STD under these angles are due to the fact, that the angle θ of the entries is taken at the vertex whereas the θ of the binning is taken at the origin of H1 coordinate system. As the vertices are distributed around z (see figures 4.3(a) and 4.3(b)) this leads to smearing or migration between different bins. So a track originating from a vertex at negative z and small θ might hit CJC, which it would not if the vertex was at $z = 0$. This is a disadvantage of plotting just θ, for further analysis it would be nice to plot directly the tracks with hits in the different detectors.

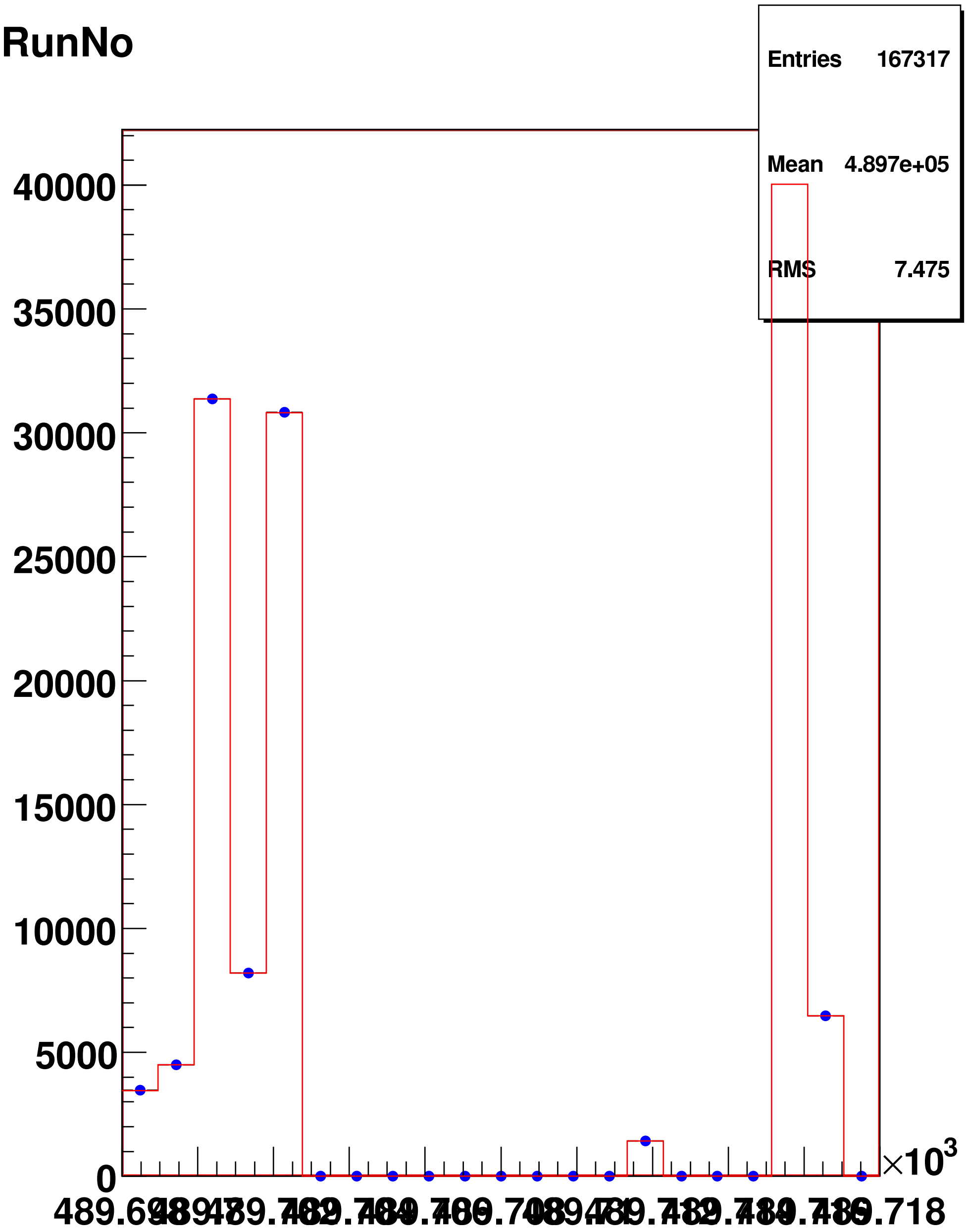

Figure 4.2: Comparison of STD (bars) and IMP (dots) concerning the run numbers the events belong to.

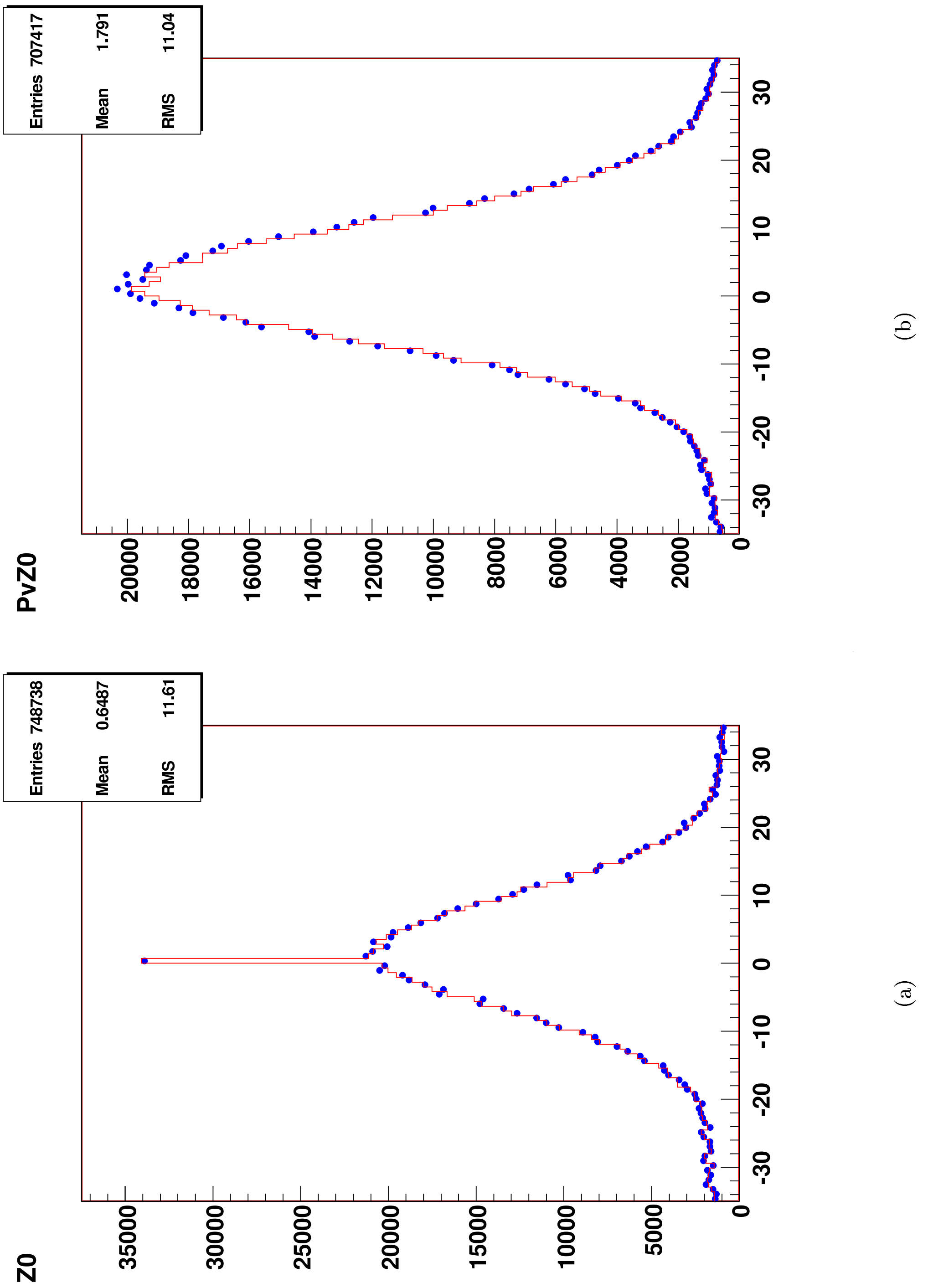

(a)

(b)

Figure 4.3: Comparison of STD (bars) and IMP (dots) for non vertex (a) and for PV (b) fitted tracks concerning the positon of the vertex z_0 [cm].

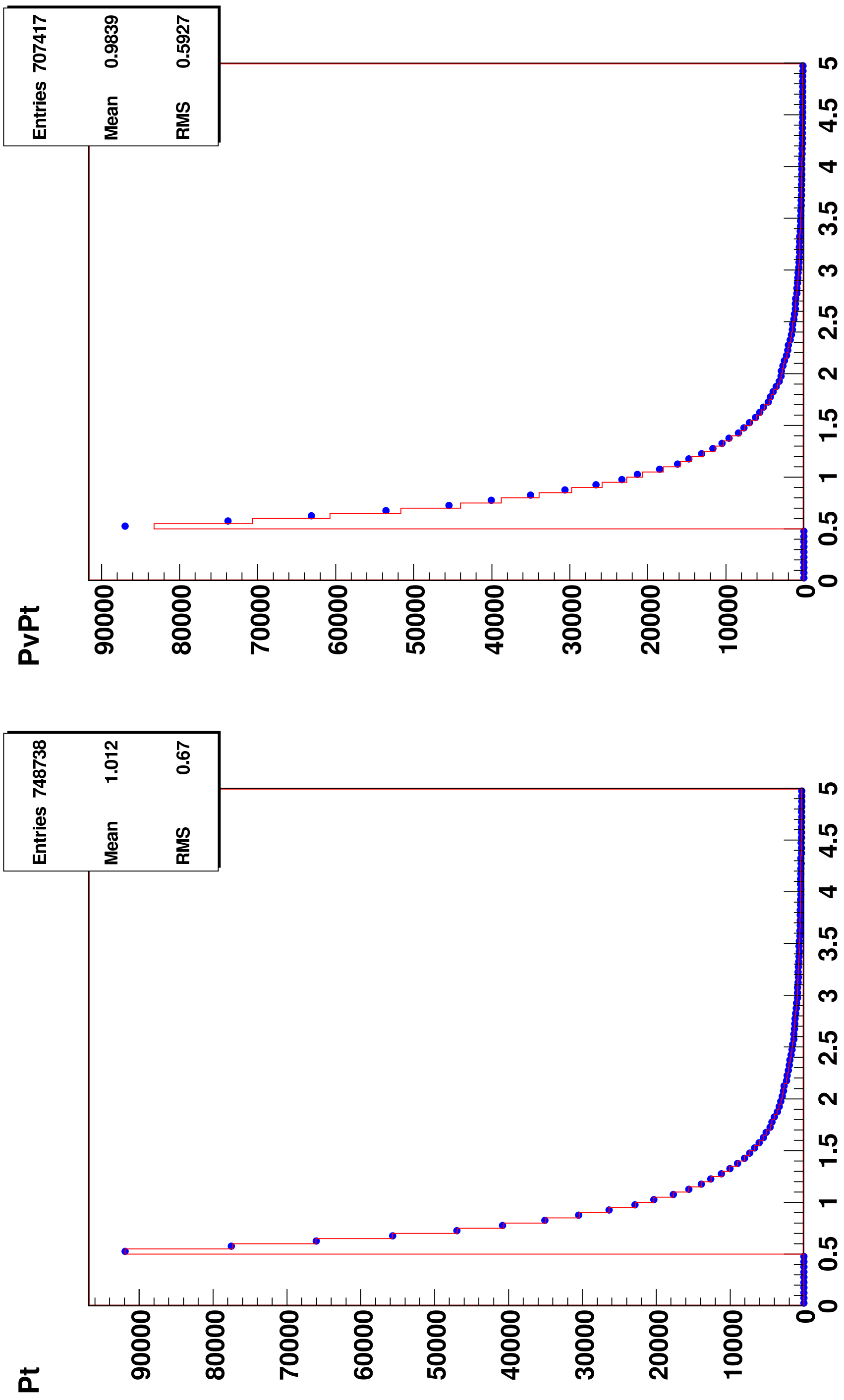

(a)

(b)

Figure 4.4: Comparison of STD (bars) and IMP (dots) for non vertex (a) and for PV (b) fitted tracks concerning the transverse momentum p_T [GeV].

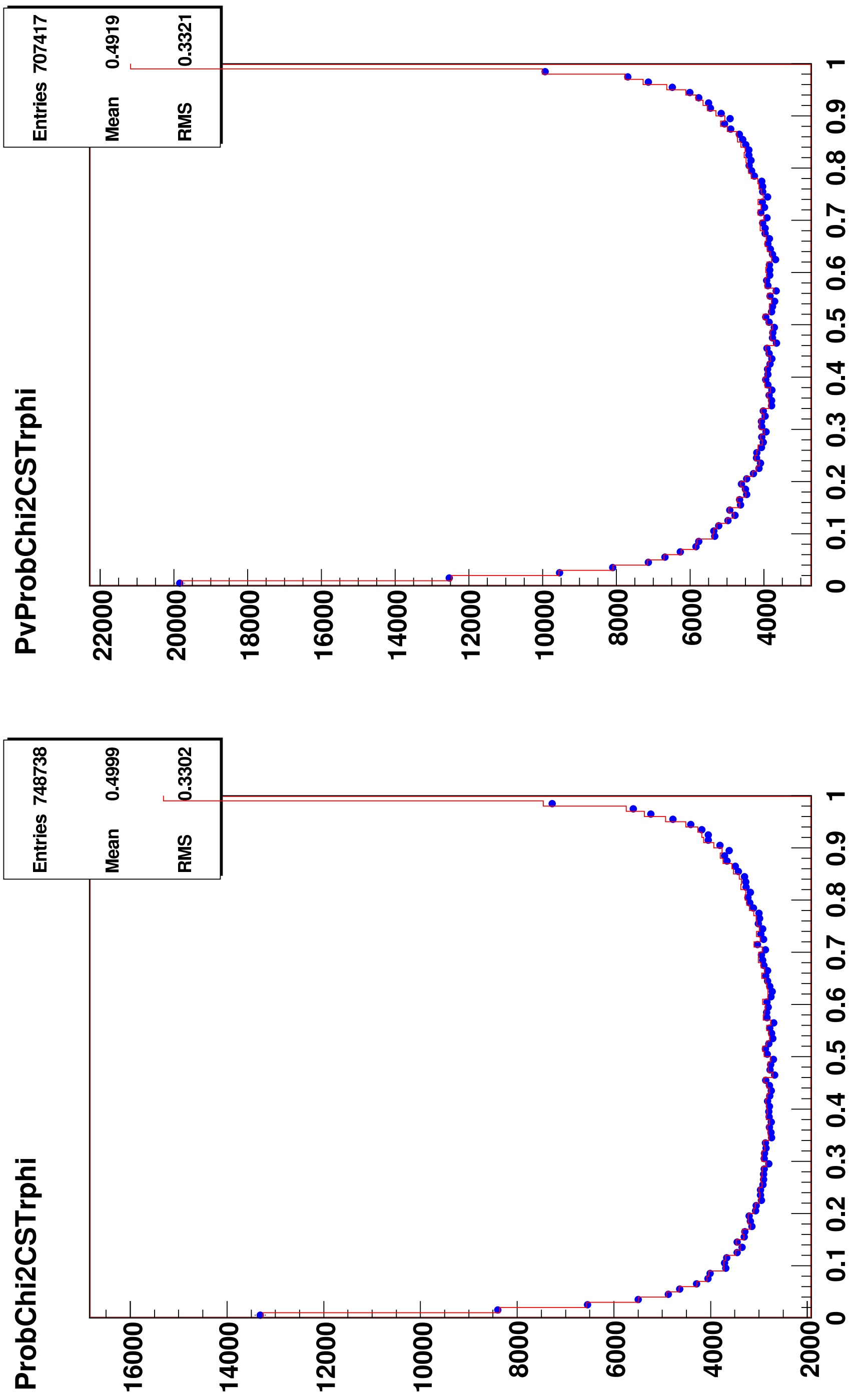

(b)

(a)

Figure 4.5: Comparison of STD (bars) and IMP (dots) for non vertex (a) and for PV (b) fitted tracks concerning ProbChi function [].

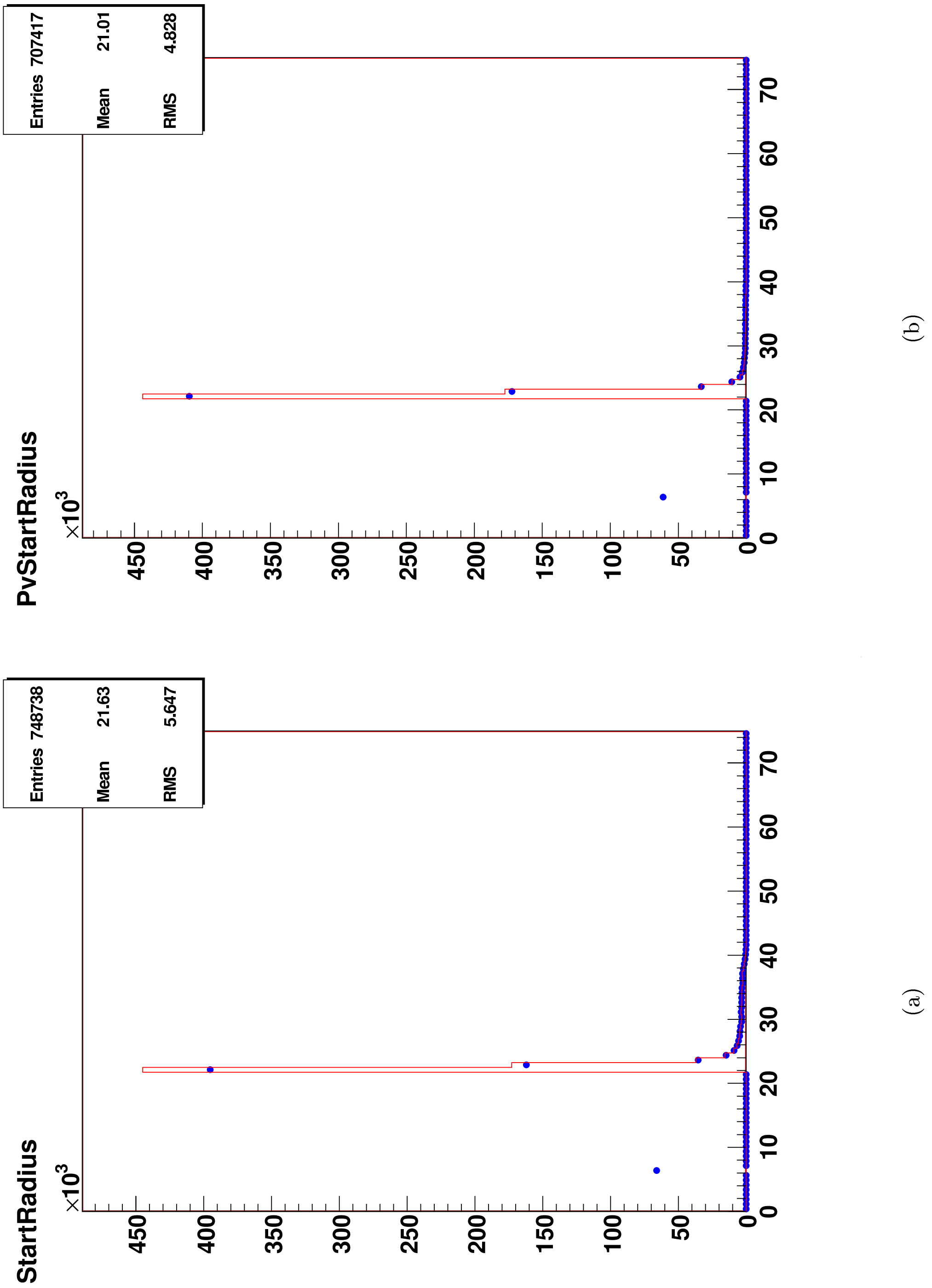

(a)

(b)

Figure 4.6: Comparison of STD (bars) and IMP (dots) for non vertex (a) and for PV (b) fitted tracks concerning the radius [cm] of the first track hit in the H1 coordinate system.

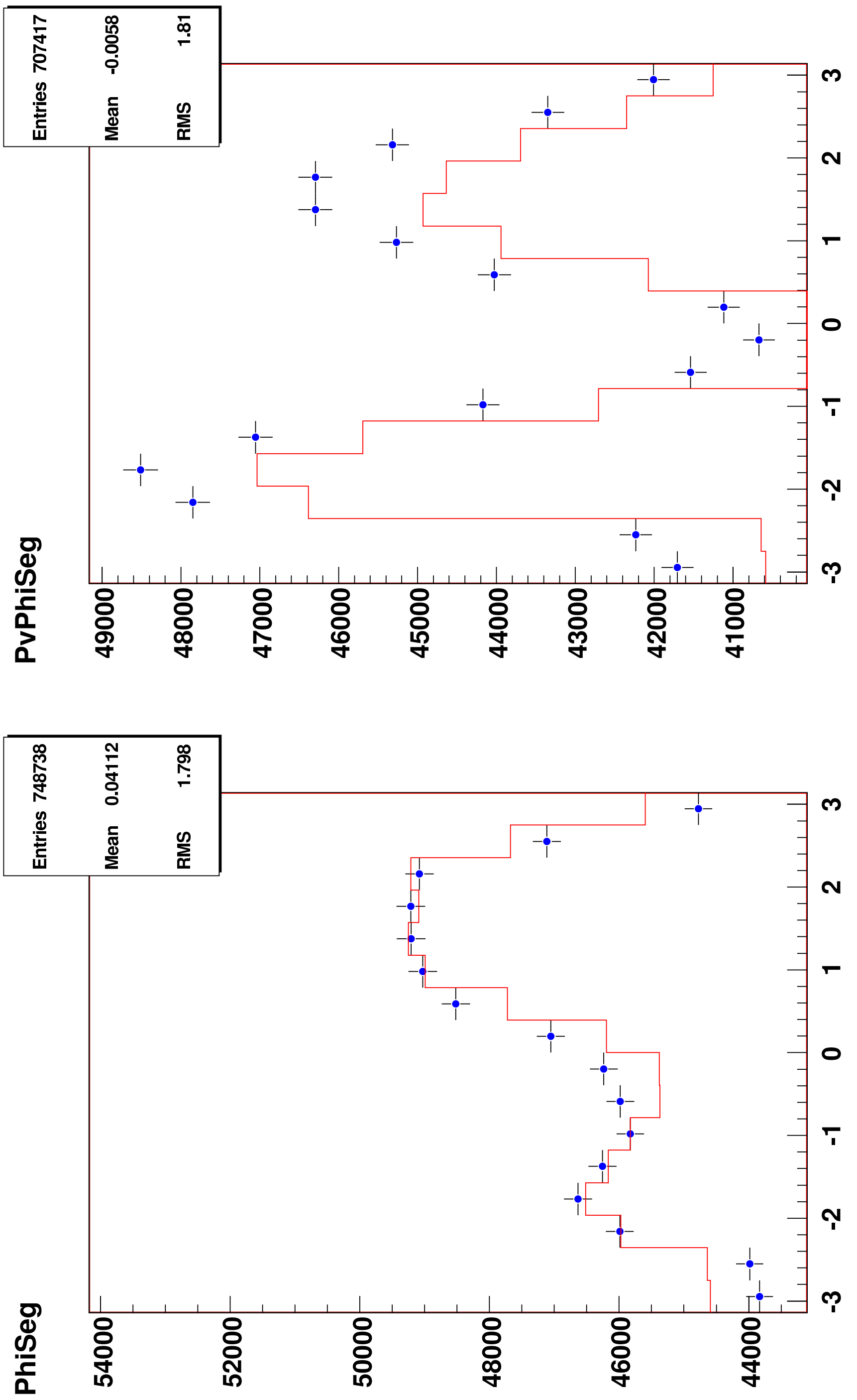

(a)

(b)

Figure 4.7: Comparison of STD (bars) and IMP (dots) for non vertex (a) and for PV (b) fitted tracks concerning the distribution of the azimuthal angle φ [].

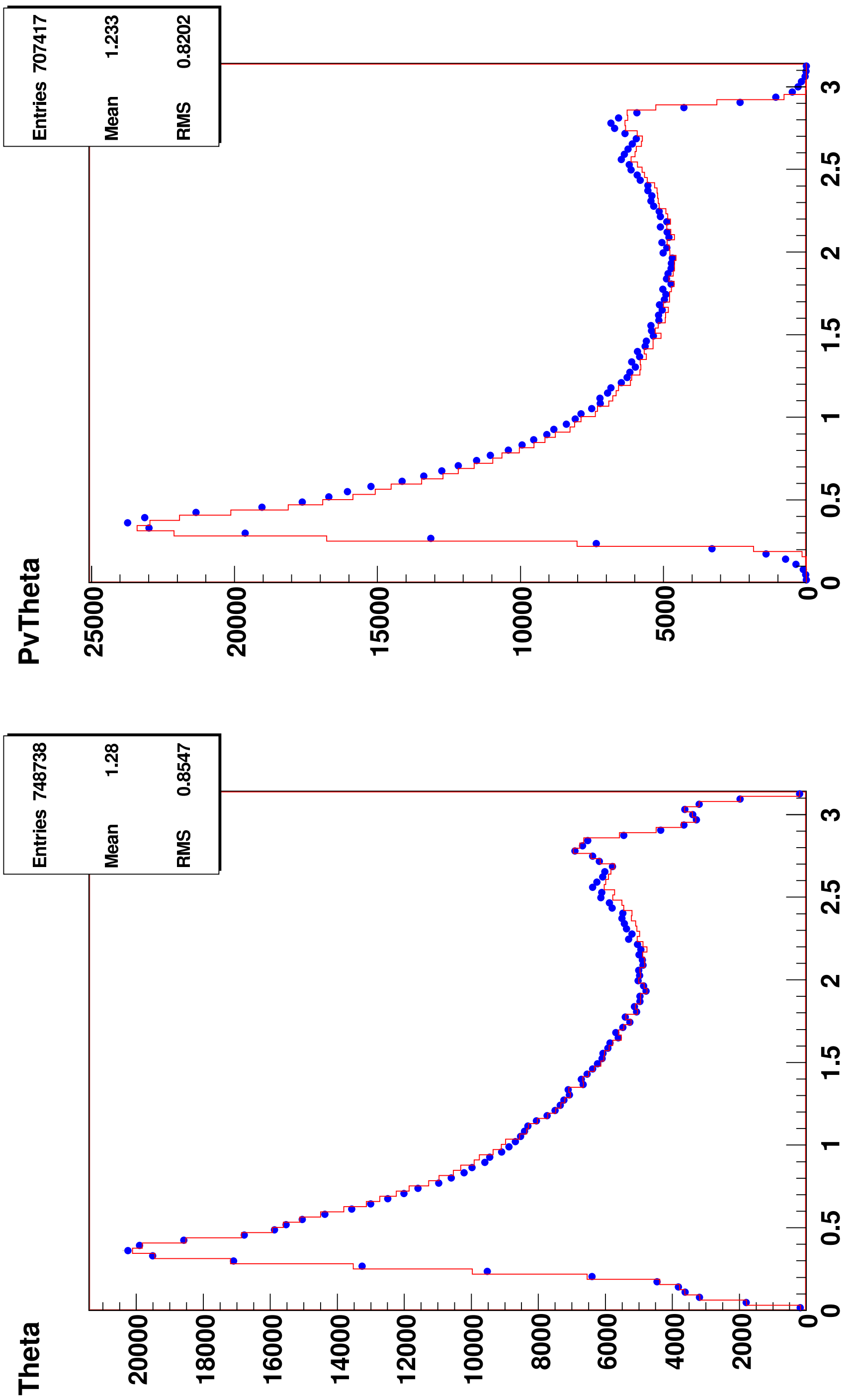

(a)

(b)

Figure 4.8: Comparison of STD (bars) and IMP (dots) for non vertex (a) and for PV (b) fitted tracks concerning the distribution of the polar angle θ [].

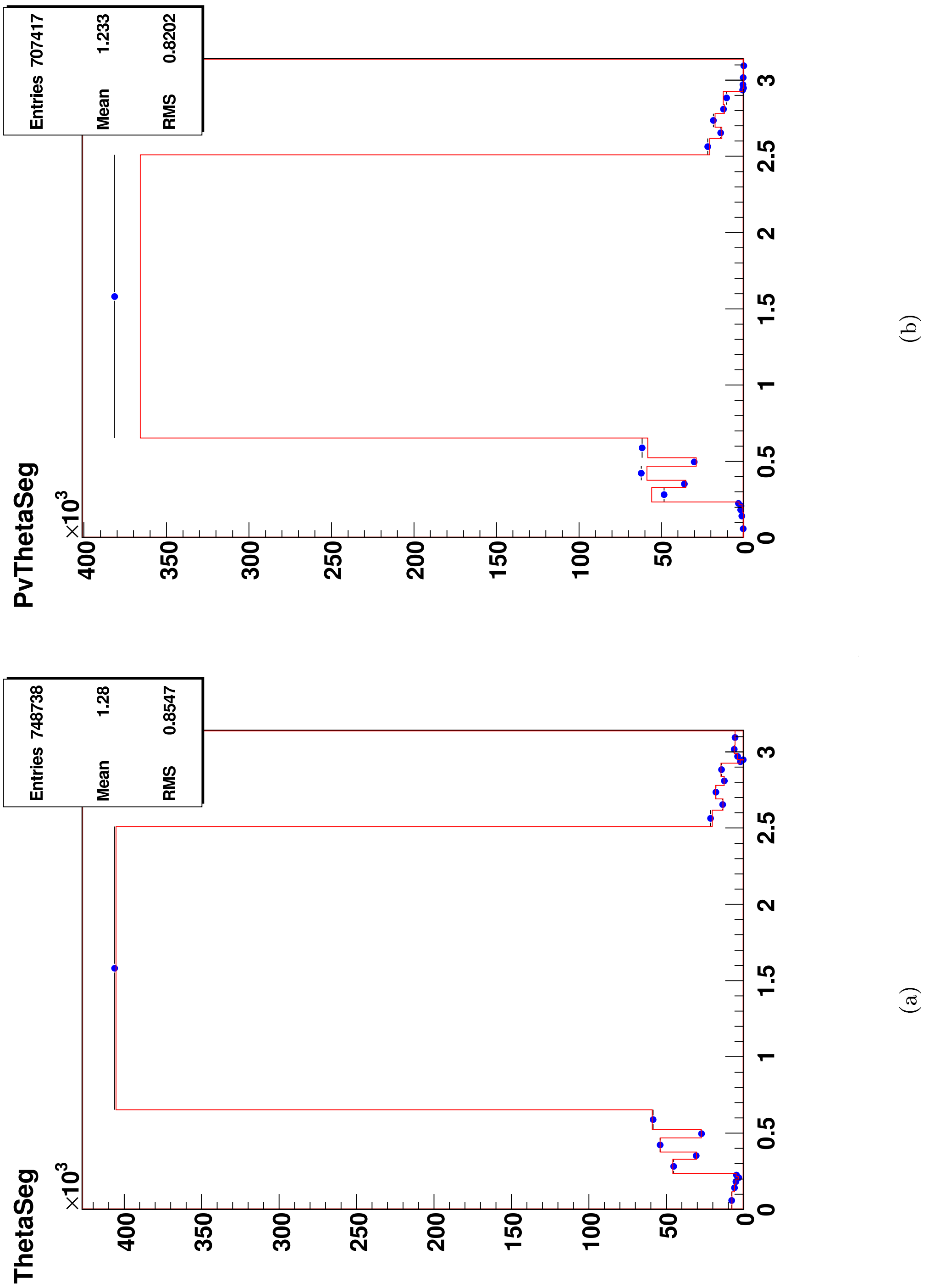

(a)

(b)

Figure 4.9: Comparison of STD (bars) and IMP (dots) for non vertex (a) and for PV (b) fitted tracks concerning the distribution of the polar angle θ [].

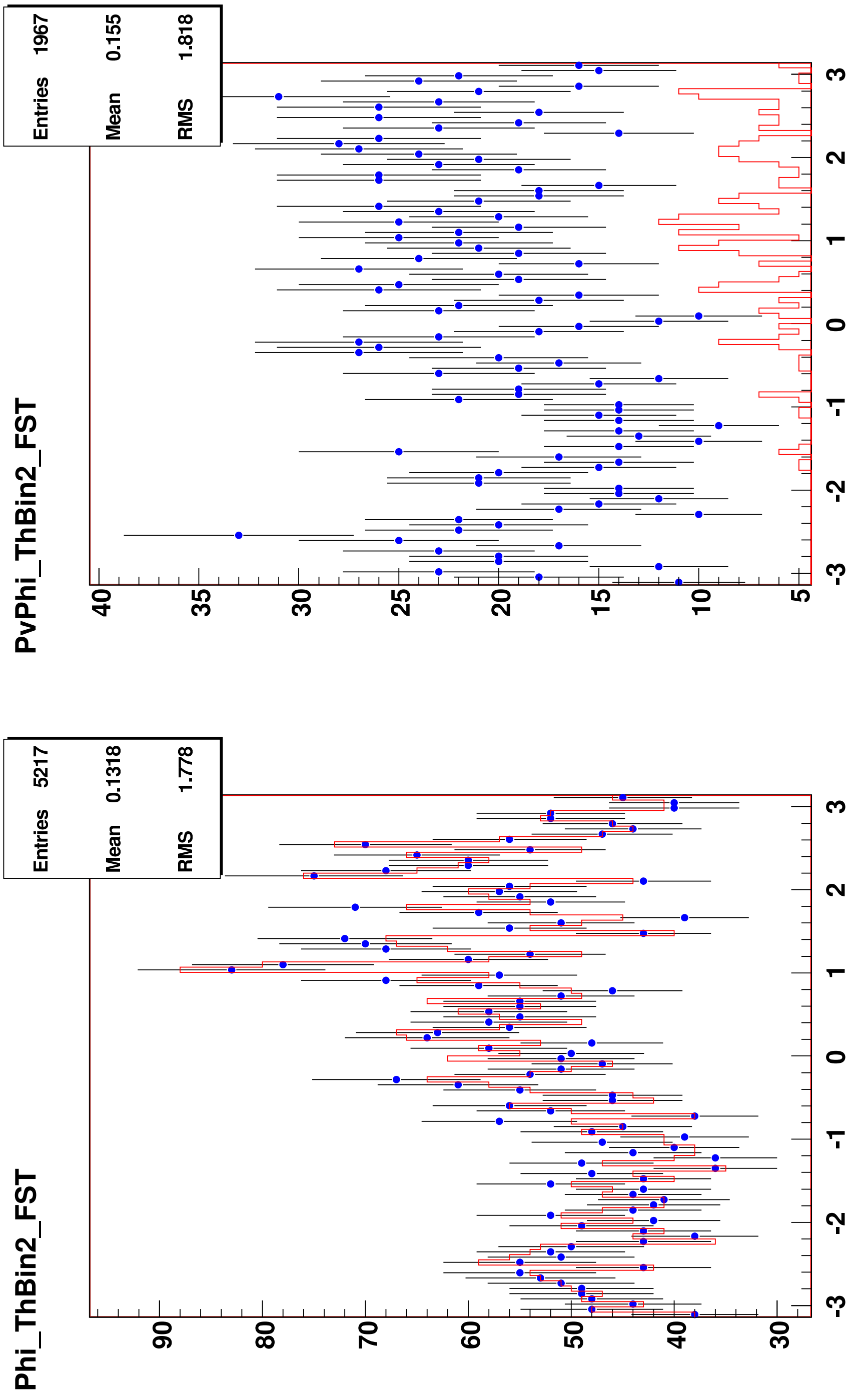

(a)

(b)

Figure 4.10: Comparison of STD (bars) and IMP (dots) for non vertex (a) and for PV (b) fitted tracks concerning the distribution of the azimuthal angle φ [] within the bin, where FST is fully sensitive but no other detectors.

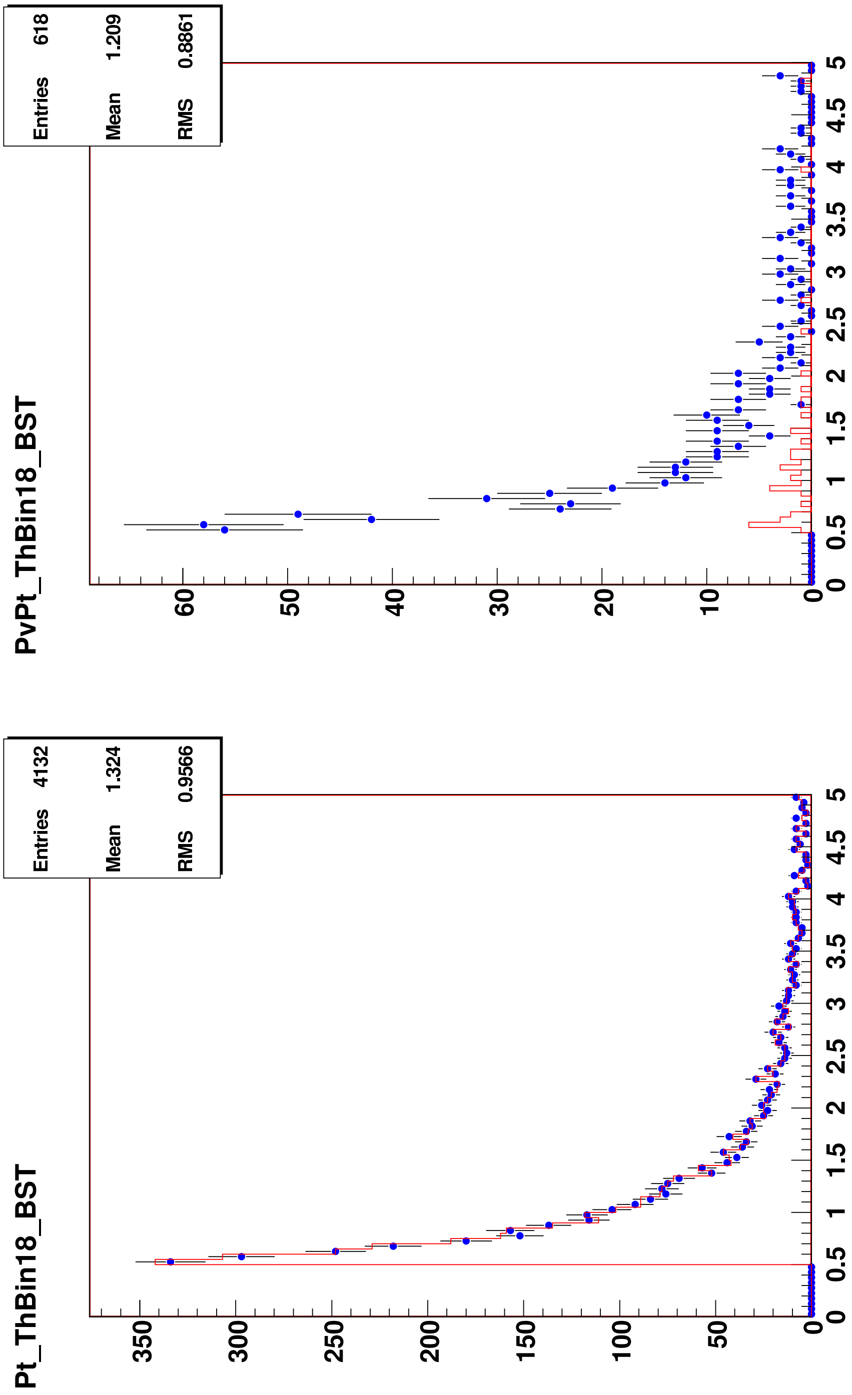

(b)

(a)

Figure 4.11: Comparison of STD (bars) and IMP (dots) for non vertex (a) and for PV (b) fitted tracks concerning the distribution of the transversal momentum p_T [GeV] within the bin, where BST is fully sensitive but no other detectors.

4.3.2 Comparison of PSCC Events

The data analysed in this section are preselected PSCC events reconstructed by R. Placakyte [1] (exclusive sample). As in the previous section, STD and IMP track reconstruction are compared, where the bars always denote STD, the points IMP data. No normalization has been applied.

In figure 4.12 one can see, that for some runs the two reconstruction methods do not select the same events for all runs, mainly IMP does not select all events that STD selects as it should. It has been checked if that difference exists for another run range as well (i.e. if there is a hardware problem with some runs). The difference remains. Therefore the error has to be searched for either in the S. Gorbounov package that provides FST/BST analysis, or in the implementation of Gorbounovs package into STD reconstruction – or it is a systematic problem of PSCC. Work on that problem is going on. As there are less events selected for further track analysis in IMP compared to STD, it is expected that less tracks are found as well for all following histograms. The histograms are then here normalized to the number of entries, and do not show the absolute values due to this problem.

Same as for the inclusive sample in figures 4.4(a), 4.4(b), 4.5(a), 4.5(b), 4.3(a) and 4.3(b) are shown in figures 4.13(a), 4.13(b), 4.14(a), 4.14(b), 4.15(a) and 4.15(b) the corresponding distributions of the transverse momentum, the function ProbChi and of the position of the vertex. It can be seen, that within the selected events IMP detects the same tracks as STD does.

Another problem of the PSCC event sample is that the radius of each track starts with the CJC1, as shown in figures 4.16(a) and 4.16(b). This implies that there is a hidden cut while producing the PSCC event itself, as this effect was not seen with the inclusive sample. A large fraction of tracks, about 20 %, are then rejected due to this cut.

The peak at ~ 22 cm comes from the CJC as expected.

In contrast to an inclusive event selection (see figures 4.8(a) and 4.8(b)), PSCC events (figures 4.17(a) and 4.17(b)) show a dissatisfying θ distribution, mainly for FST/BST sensitive angles no more tracks are detected by IMP. The explanation is the cut in the PSCC package mentioned above. This problem remains also after normalizing to the same number of selected events. As a consequence, IMP can not yet been used to replace STD completely for PSCC events as it is now.

Figure 4.18(a) shows a θ plot with the special binning explained in section 4.2.1, where in each bin different detectors are sensitive. The figures 4.19(a), 4.19(b), 4.20(a) and 4.20(b) show examples for φ and p_T distributions respectively for two bins, where only FST and BST respectively are sensitive. Together with the plots of other bins they might contribute to a clarification, how IMP could be adapted for PSCC analysis such that IMP could completely replace STD.

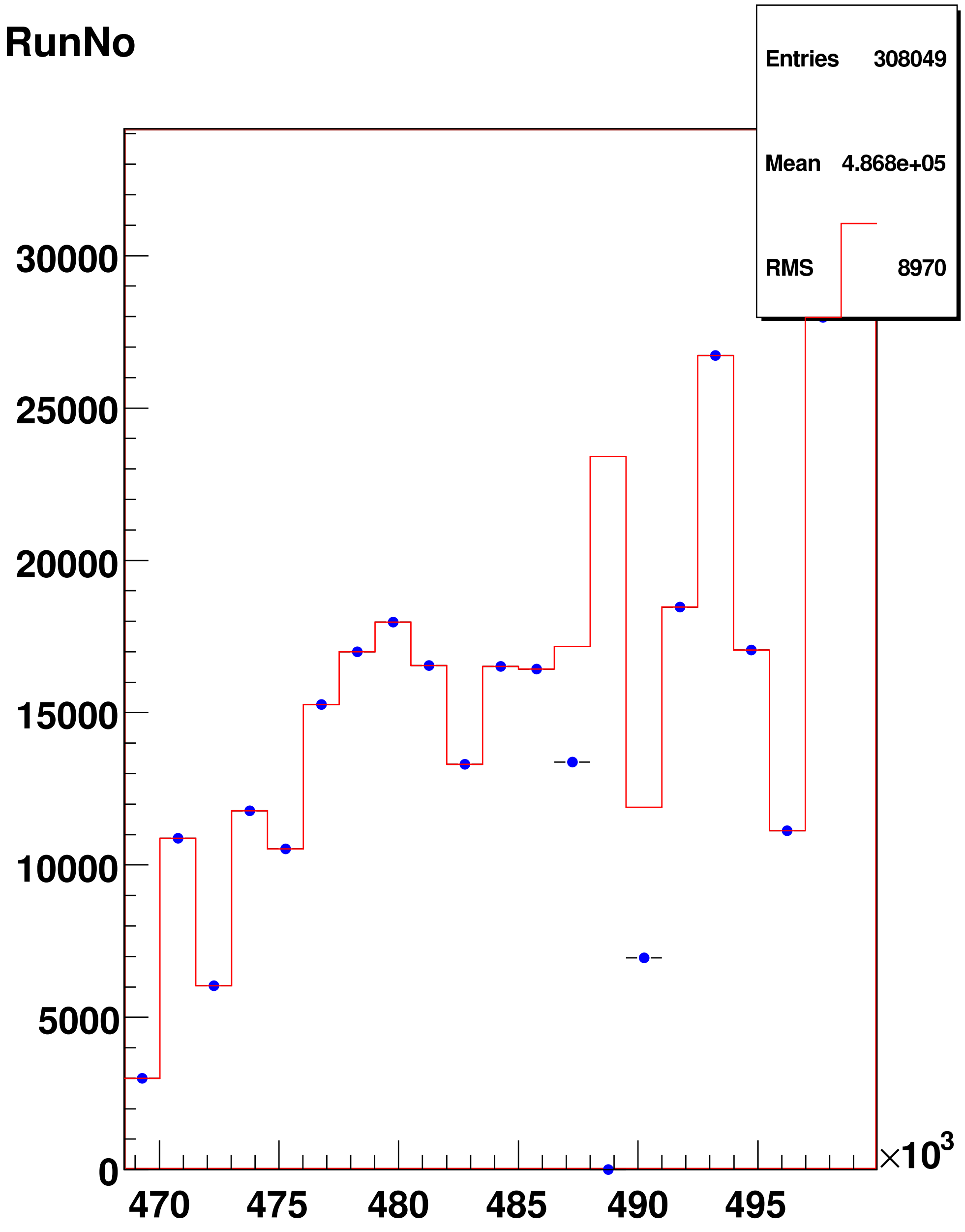

Figure 4.12: Comparison of STD (bars) and IMP (dots) for PSCC events concerning the run numbers the events belong to.

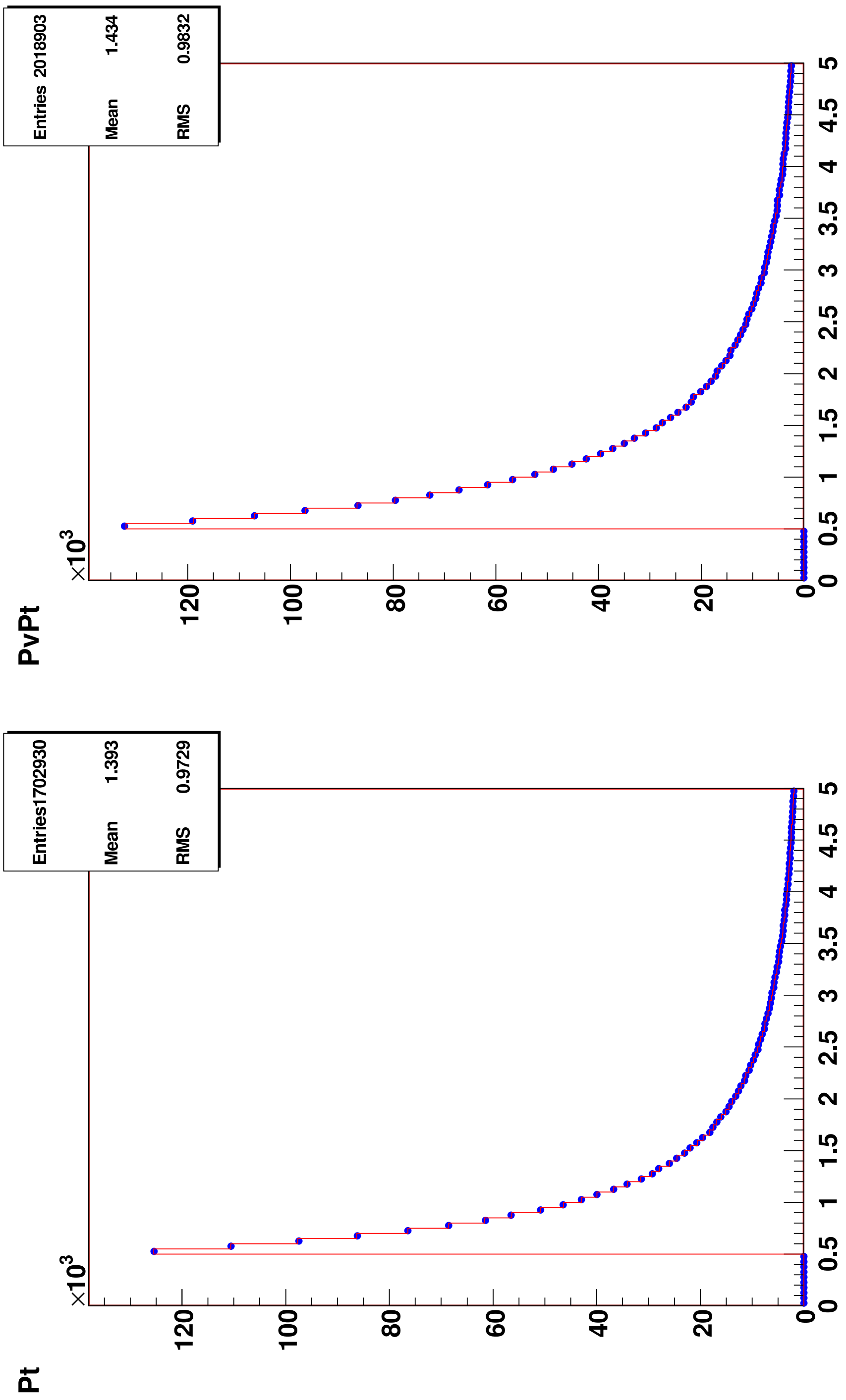

(a)

(b)

Figure 4.13: Comparison of STD (bars) and IMP (dots) for PSCC events (non vertex (a) and PV (b) fitted tracks) concerning the transverse momentum p_T [GeV].

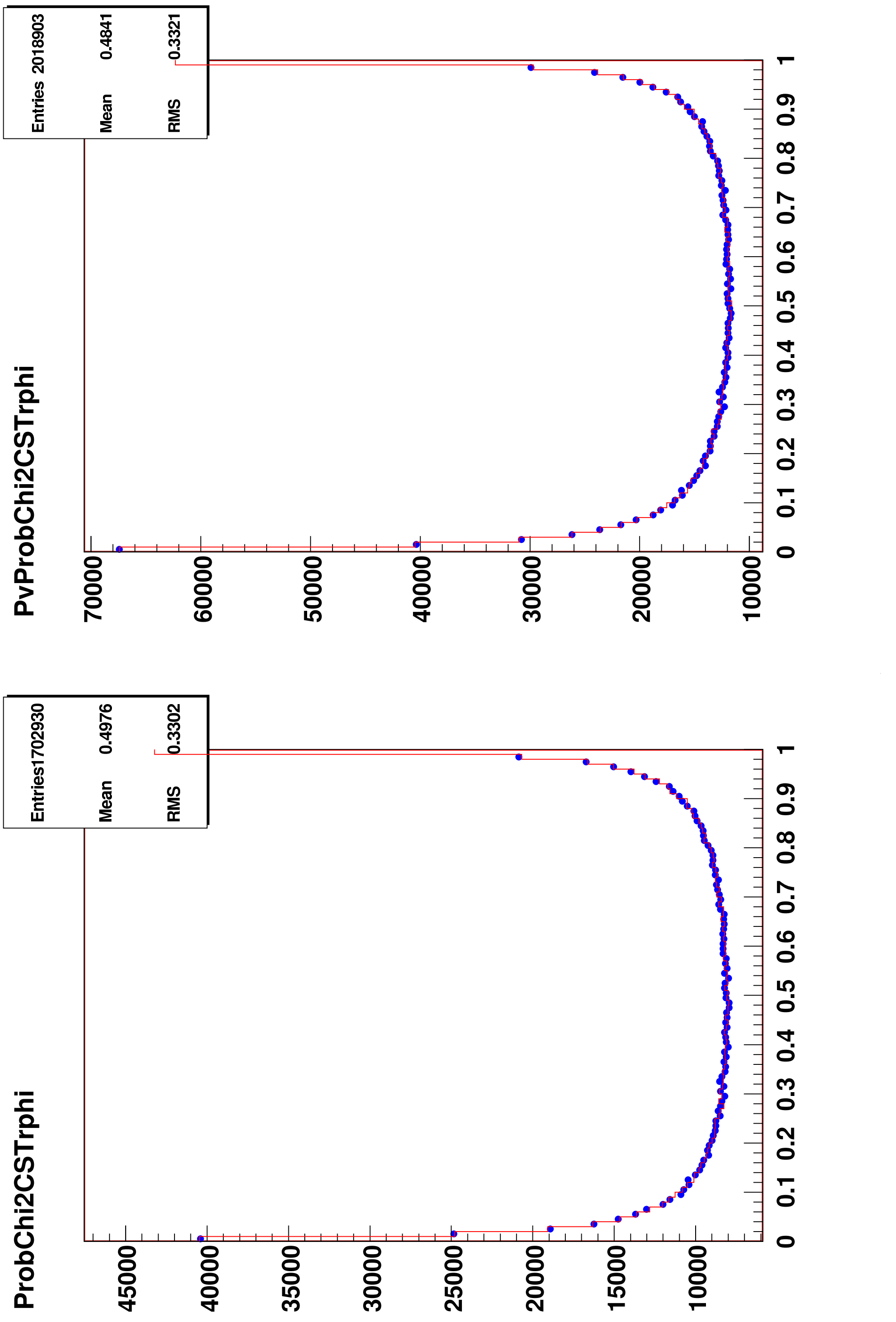

(a)

(b)

Figure 4.14: Comparison of STD (bars) and IMP (dots) for PSCC events (non vertex (a) and PV (b) fitted tracks) concerning the ProbChi function [].

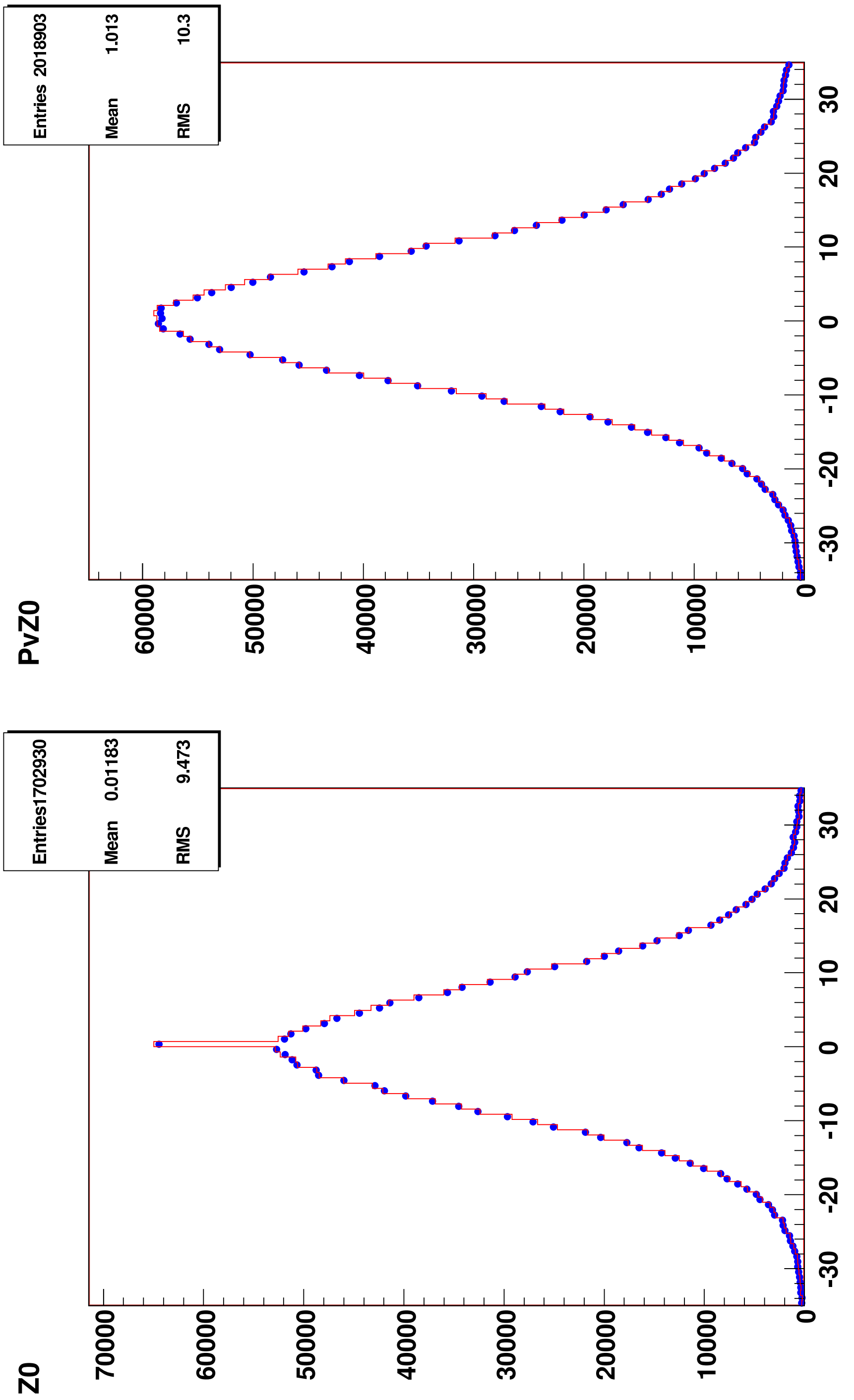

(a)

(b)

Figure 4.15: Comparison of STD (bars) and IMP (dots) for PSCC events (non vertex (a) and PV (b) fitted tracks) concerning the positon of the vertex z_0 [cm].

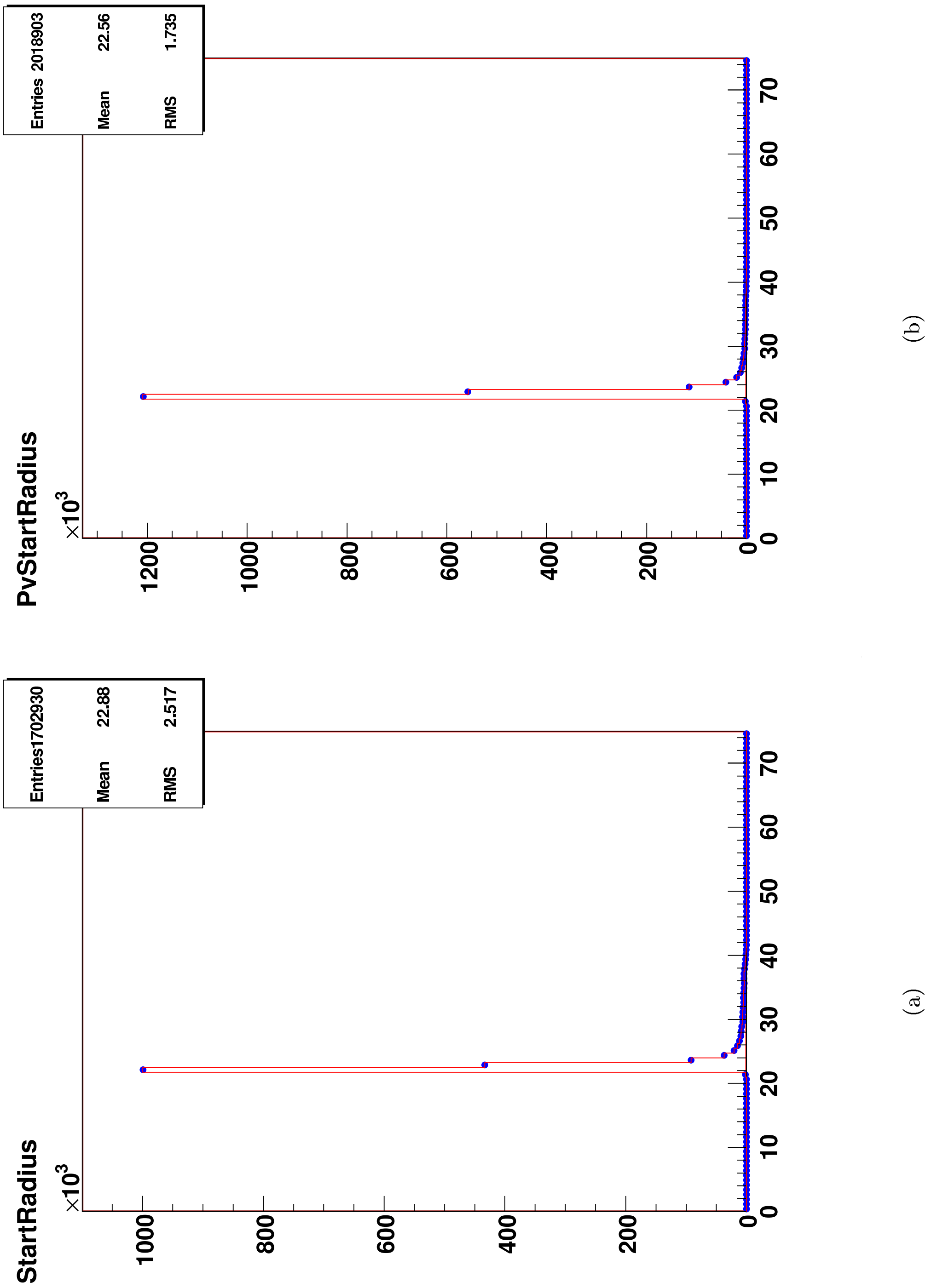

(a)

(b)

Figure 4.16: Comparison of STD (bars) and IMP (dots) for PSCC events (non vertex (a) and PV (b) fitted tracks) concerning the radius [cm] of the first track hit in the H1 coordinate system.

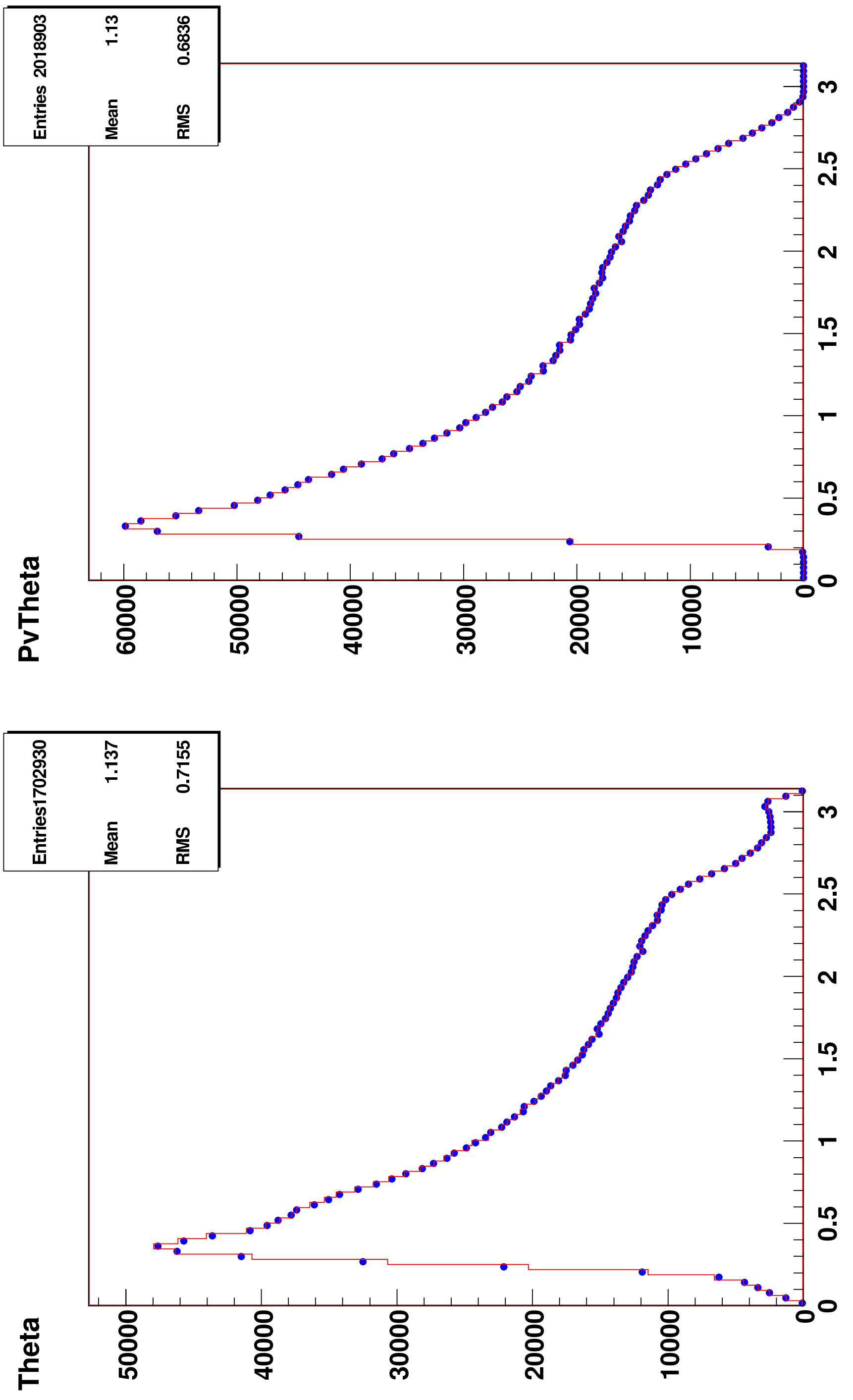

(b)

(a)

Figure 4.17: Comparison of STD (bars) and IMP (dots) for PSCC events (non vertex (a) and PV (b) fitted tracks) concerning the distribution of the polar angle θ [].

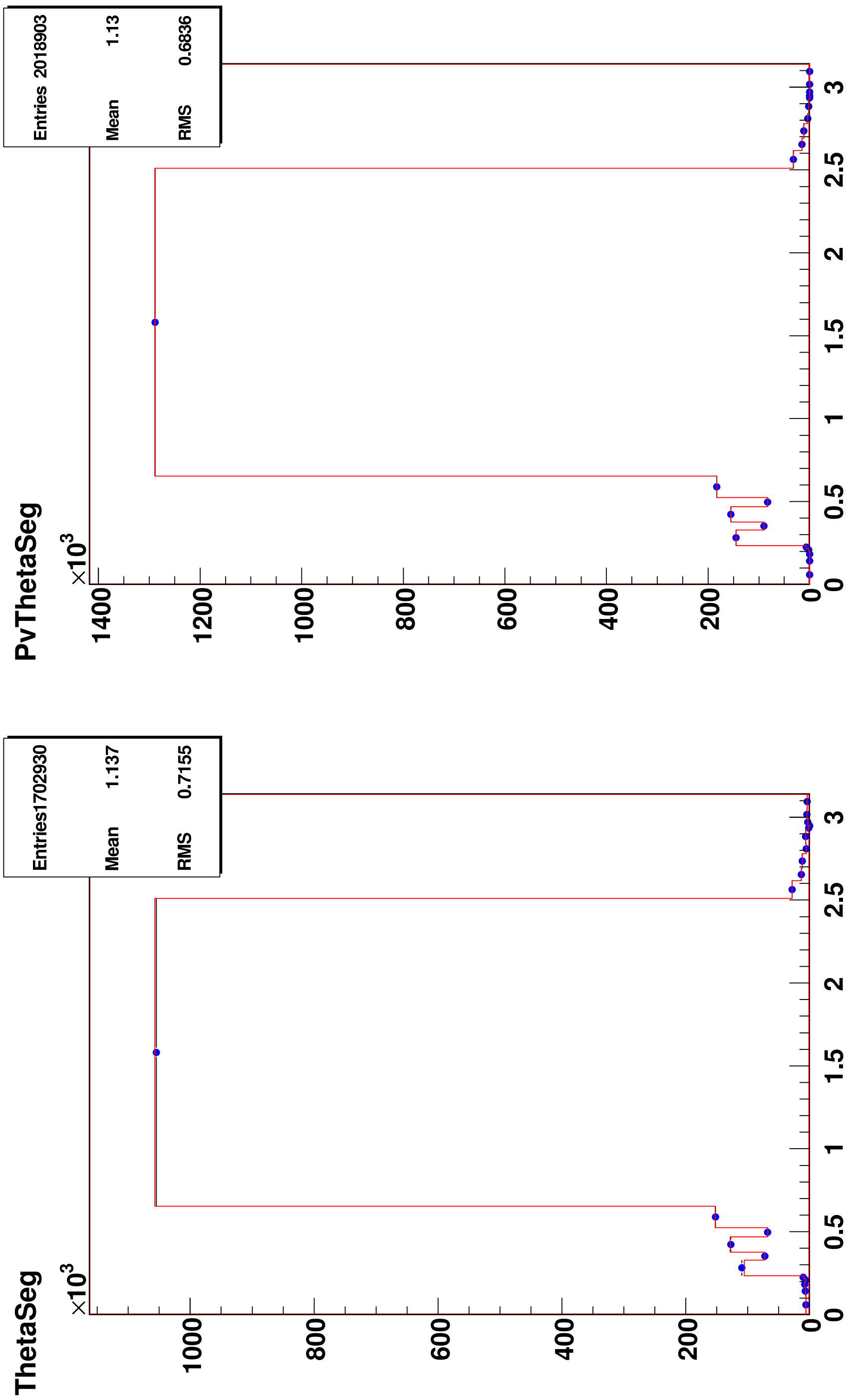

(b)

(a)

Figure 4.18: Comparison of STD (bars) and IMP (dots) for PSCC events (non vertex (a) and PV (b) fitted tracks) concerning the distribution of the polar angle θ [].

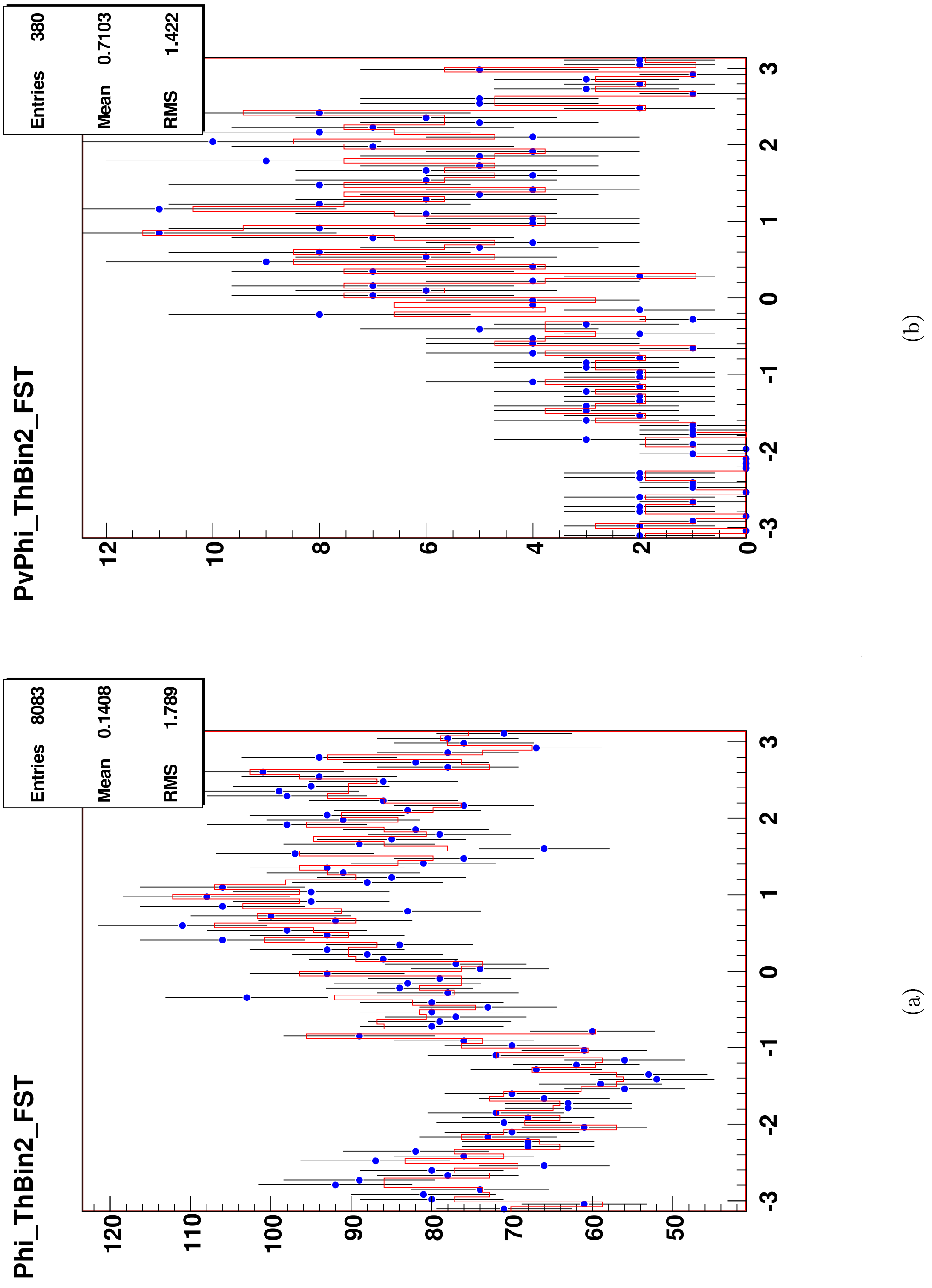

(a)

(b)

Figure 4.19: Comparison of STD (bars) and IMP (dots) for PSCC events (non vertex (a) and PV (b) fitted tracks) and PV 4.19(b) tracks) concerning the distribution of the azimuthal angle φ [] within the bin, where FST is fully sensitive but no other detectors.

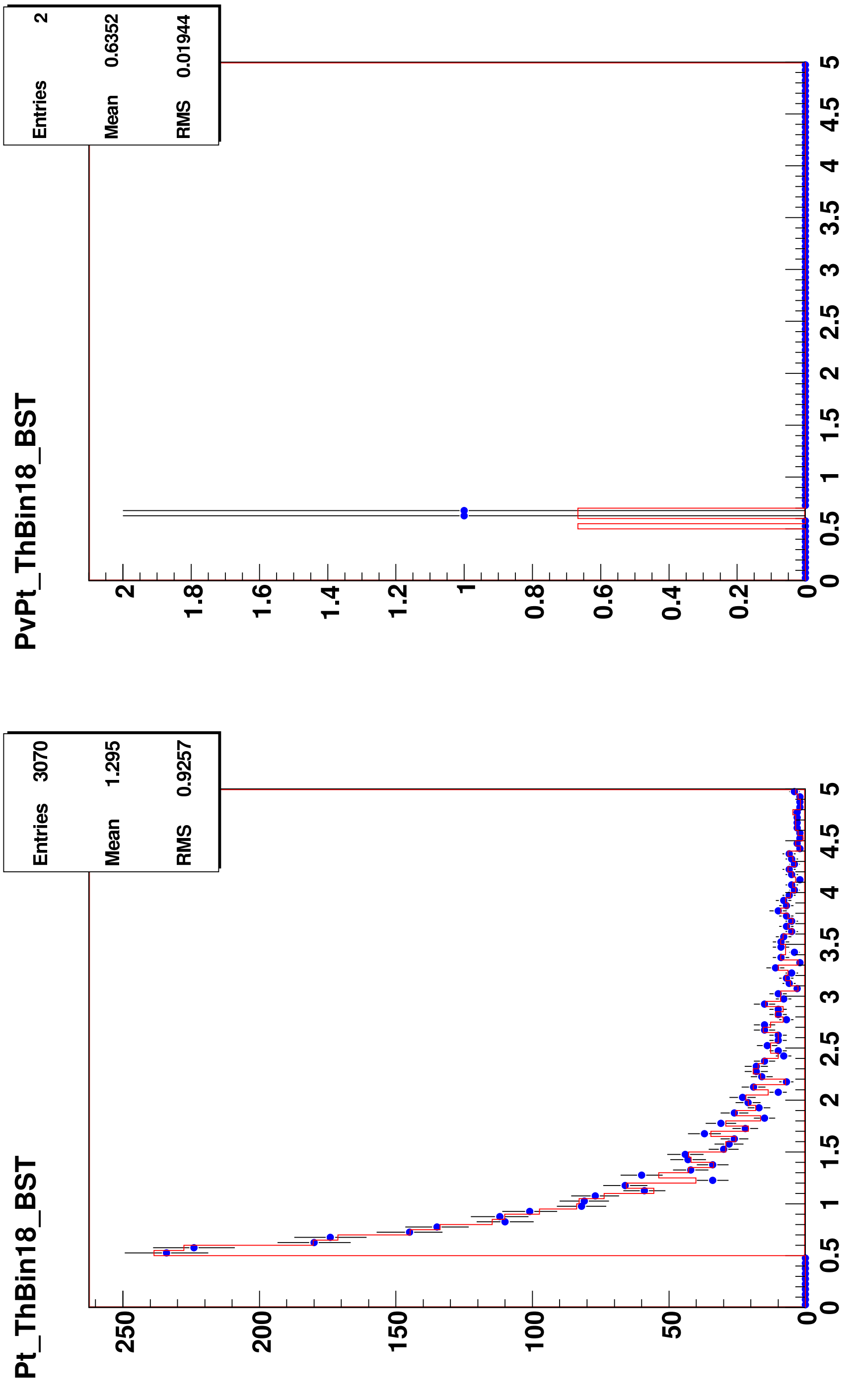

(a)

(b)

Figure 4.20: Comparison of STD (bars) and IMP (dots) for PSCC events (non vertex (a) and PV (b) fitted tracks) concerning the distribution of transversal momentum p_T [GeV] within the bin, where BST is fully sensitive but no other detectors.

5 Conclusion and Outlook

The presented analysis shows, that the improvement of the track reconstruction is clearly worthwile. More primary vertex fitted tracks are found which results in higher statistics. Discussions are now going on to check the new construction on physics samples and to fix the remaining problems. Open questions are:

- Why is a loss of events in PSCC observed?
- How can events be selected that have no hits in CJC1, which means selection via BST or FST standalone tracks?
- Why is ProbChi not flat?
- Why are no tracks seen in PSCC that start in FST/BST?

Due to higher selection efficiency for the inclusive event sample it can be expected that after answering the above questions, IMP is a good alternative to STD with integration of FST and BST detectors.
This should go to the official H1 reconstruction software for the next reprocessing of the HERA II data, schedule end of this year.

Acknowledgements

I would like to thank first my supervisor Guillaume Leibenguth, who stimulated me a lot and was able to transmit his enthusiasm for the project on me. He always had time when I did not understand and was willing to explain, but also letting enough freedom to let me find solutions by myself.

I would like to thank to my colleagues Michel Sauter and Roger Haelg, who helped me always when I did not understand what I was doing wrong and with whom it was just very comfortble to share the office.

Finally I would like to thank to the people from DESY who gave me the possibility to participate in the Summer Students Program 2007 and to Christoph Grab and Jürgen Ulbricht, who wrote successfully recommendations for me.

List of Figures

Bibliography

[1] R. Placakyte, First Mesurement of Charged Current Cross Sections with Longitudinally Polarised Positrons at HERA, PhD Thesis, www-h1.desy.de/psfiles/theses/h1th-455.ps.

[2] I. Abt *et al.*, H1 collaboration, The H1 Detector at HERA, Nucl. Instr. Meth. **A386** (1997), 310-347.

[3] B. List, The H1 Central Silicon Tracker, Nucl. Instr. and Meth. **A501** (2003) 49-53.

[4] B. List, The H1 Silicon Tracker, Nucl. Instr. and Meth. **A549** (2005) 33-36.

[5] W. Braunschweig *et al.*, A Forward Silicon Tracker for H1, H1-02/99-563 (H1 internal report), https://www-h1.desy.de/idet/upgrade/silicon/fst/fstprc-9901.ps.

[6] M. Nozicka, Forward Silicon Tracker of the H1 Experiment: Hardware and Study of D^* Meson Detection, PhD Thesis.

[7] D. Pitzl *et al.*, The H1 Silicon Vertex Detector, Nucl. Inst. and Meth. **A454** (2000) 334-349.

[8] W. Erdmann, S. Mangano, CST Geometry Description, https://www-h1.desy.de/idet/itracker/isitracker/icst/reconstruction/cst_geometry.ps.gz.

[9] H1 collaboration, https://www-h1.desy.de/idet/itracker/isitracker/icst/reconstruction/index.html.

[10] O. Behnke, CSTREC Operations on CST Hits, https://www-h1.desy.de/idet/itracker/isitracker/icst/reconstruction/CSThits/CSThits.ps.gz.

[11] I.J.R. Aitchison and A.J.G. Hey, Gauge Theories in Particle Physics, Adam Hilger LTD, Bristol (1982) 333 p.

[12] A. Dubak, Measurement of the e^+p Neutral Current DIS Cross Section and F_2, F_L, xF_3 Structure Functions in the H1. Experiment at HERA, PhD Thesis, LMU München (2003)

[13] F. Keil, Dijet Production in Charged and Neutral Current e^+p Interactions at High Q^2 at HERA, PhD Thesis, Heidelberg (2001).

[14] A. Meyer, http://www.desy.de/ ameyer/hq/node25.html.

[15] H1 collaboration, https://www-h1.desy.de/icas/oop/.

[16] H1 collaboration, The H1 OO Physics Analysis Project, https://www-h1.desy.de/icas/oop/current/userguide.

[17] http://root.cern.ch/.

[18] H1 collaboration, https://www-h1.desy.de/icas/imanuals/h1rec/h1rec9/h1rec.html.

[19] G. Leibenguth, D. Pitzl, private communication.

[20] G. Leibenguth, The H1 Silicon Tracker, talk given at 9^{th} ICATPP, Como (2005).